J|A|C|S
ARTICLES

Published on Web 08/26/2009

On the XeF^+/H_2O System: Synthesis and Characterization of the Xenon(II) Oxide Fluoride Cation, $FXeOXeFXeF^+$

Michael Gerken,[†,‖] Matthew D. Moran,[†] Hélène P. A. Mercier,[†] Bernard E. Pointner,[†]
Gary J. Schrobilgen,[*,†] Berthold Hoge,[‡,⊥] Karl O. Christe,[*,‡] and Jerry A. Boatz[§]

Department of Chemistry, McMaster University, Hamilton ON L8S 4M1, Canada, Loker Hydrocarbon Research Institute and Department of Chemistry, University of Southern California, Los Angeles, California 90089, and Air Force Research Laboratory, Edwards Air Force Base, California 93524

Received June 19, 2009; E-mail: schrobil@mcmaster.ca; kchriste@usc.edu

Abstract: The reported synthesis of the H_2OF^+ cation as a product of the oxidative fluorination of H_2O by $[XeF][PnF_6]$ (Pn = As, Sb) in HF solution has been reinvestigated. The system exhibits complex equilibria, producing two new Xe(II) compounds, $[Xe_3OF_3][PnF_6]$ and $[H_3O][PnF_6]\cdot2XeF_2$, refuting the original claim for the synthesis of the H_2OF^+ cation. Both compounds have been isolated and characterized by vibrational spectroscopy and single-crystal X-ray diffraction. The X-ray crystal structures of the $[Xe_3OF_3][PnF_6]$ salts contain the *Z*-shaped $FXeOXeFXeF^+$ cation, which represents the first example of an isolated Xe(II) oxide fluoride. The crystal structure of the $[H_3O][AsF_6]\cdot2XeF_2$ adduct contains XeF_2 molecules that interact with the H_3O^+ cations. The vibrational assignments for the $Xe_3OF_3^+$ cation have been made with the aid of quantum-chemical calculations and were confirmed by ^{18}O-enrichment, and the assignments for $[H_3O][AsF_6]\cdot2XeF_2$ were confirmed by ^2D- and ^{18}O-enrichment. Quantum-chemical calculations have also been carried out for $H_3O^+\cdot nXeF_2$ ($n = 1-4$) and have been used to interpret the X-ray crystal structure and vibrational spectra of $[H_3O][AsF_6]\cdot2XeF_2$. The energy-minimized geometries and vibrational frequencies for HOF and H_2OF^+ have been calculated, further disproving the original report of the H_2OF^+ cation. Both FXeOH and $FXeOH_2^+$ have also been computed and are viable intermediates in the proposed equilibria between XeF^+ and H_2O that lead to the $Xe_3OF_3^+$ cation.

Introduction

Chlorine oxide pentafluoride, $ClOF_5$, would be the highest performing earth-storable, liquid rocket-propellant oxidizer. Although the synthesis of $ClOF_5$ had been claimed in 1972,[1] this claim was subsequently refuted.[2] Continued efforts to prepare this compound by oxidative fluorination of substrates such as $ClOF_3$[3-5] or $ClOF_4^-$[6,7] have failed because the oxygen ligand is more easily oxidized than the central chlorine atom. This failure prompted a search for alternate synthetic approaches, such as the reaction of ClF_5 with an oxidative oxygenator. Potential candidates for oxidative oxygenators include hypofluorous acid, HOF, a well-known unstable compound,[8,9] and its protonated form, the H_2OF^+ cation,[10,11] if indeed it should exist. It was claimed that the synthesis of the latter cation could be accomplished by the oxidative fluorination of H_2O with $[XeF][PnF_6]$ (Pn = As, Sb) in HF solution at −60 °C.[10,11] The resulting product, formulated as $[H_2OF][PnF_6]$, was reported to be pale red and was characterized by infrared and ^1H and ^{19}F NMR spectroscopy. It was of particular interest because it allegedly oxygenated ClF_3 to $ClOF_2^+$.[10,11]

Despite the remarkable oxygenating power attributed to the alleged H_2OF^+ cation,[10,11] no further reports concerning H_2OF^+ have materialized since its reported discovery, except for two Master's theses from the same laboratory,[12,13] which failed to substantiate the remarkable oxidizing power attributed by the earlier authors to their product.

This paper describes attempts to reproduce the syntheses of H_2OF^+ salts and their reactions with chlorine fluorides.[10,11] Although these attempts failed and proved that the previous

---

[†] McMaster University.

[‡] University of Southern California.

[§] Edwards Air Force Base.

[‖] Present address: Department of Chemistry and Biochemistry, The University of Lethbridge, Lethbridge AB T1K 3M4, Canada.

[⊥] Present address: Fakultät für Chemie, Universität Bielefeld, Postfach 10 01 31, D-33501 Bielefeld, Germany.

(1) Zuechner, K.; Glemser, O. *Angew. Chem., Int. Ed. Engl.* **1972**, *11*, 1094–1095.

(2) Christe, K. O.; Schack, C. J. *Adv. Inorg. Chem. Radiochem.* **1976**, *18*, 319.

(3) Christe, K. O.; Pilipovich, D.; Lindahl, C. B.; Schack, C. J.; Wilson, R. D. *Inorg. Chem.* **1972**, *11*, 2189–2192.

(4) Pilipovich, D.; Rogers, H. H.; Wilson, R. D. *Inorg. Chem.* **1972**, *11*, 2192–2195.

(5) Christe, K. O.; Curtis, E. C. *Inorg. Chem.* **1972**, *11*, 2196–2201.

(6) Christe, K. O.; Schack, C. J.; Pilipovich, D. *Inorg. Chem.* **1972**, *11*, 2205–2208.

(7) Christe, K. O.; Curtis, E. C. *Inorg. Chem.* **1972**, *11*, 2209–2211.

(8) Appelman, E. H. *Acc. Chem. Res.* **1973**, *6*, 113–117.

(9) Appelman, E. H.; Dunkelberg, O.; Kol, M. *J. Fluorine Chem.* **1992**, *56*, 199–213.

(10) Minkwitz, R.; Nowicki, G. *Angew. Chem., Int. Ed. Engl.* **1990**, *29*, 688–689.

(11) Nowicki, G. Ph.D. Thesis, Universität Dortmund, Dortmund, Germany, 1992.

(12) Schwenke, S. Diplomarbeit, Universität Dortmund, Dortmund, Germany, 1990.

(13) Zoermer, M. Diplomarbeit, Universität Dortmund, Dortmund, Germany, 1991.

10.1021/ja905060v CCC: $40.75

claims were false, they have led to the isolation and characterization of the first genuine example of a Xe(II) oxide fluoride, $FXeOXeFXeF^+$ (hereafter referred to as $Xe_3OF_3^+$), as well as the adduct, $[H_3O][AsF_6]\cdot 2XeF_2$. Neutral xenon oxide fluorides of Xe(IV) ($XeOF_2$),[14-16] Xe(VI) ($XeOF_4$,[17] XeO_2F_2[18]), and Xe(VIII) (XeO_3F_2,[19] XeO_2F_4[20]) are known, and the xenon oxide fluoride cations of Xe(VI) ($XeOF_3^+$,[21-23] XeO_2F^+,[21,22,24,25] μ-$F(XeO_2F)_2^+$[24,25]) have been synthesized by fluoride ion abstraction from the parent neutral oxide fluoride using the strong fluoride acceptors AsF_5 or SbF_5. Prior to this work, no systematic study of the hydrolytic behavior of Xe(II) fluoride species had been performed, though it has been noted that aqueous solutions of XeF_2 are stable for short periods of time,[26] and no examples of neutral or ionic Xe(II) oxide fluorides had been isolated and reported.

Results and Discussion

Syntheses and Properties. To elucidate the true products of the reaction of H_2O with XeF^+, NMR spectroscopy was used to characterize HF solutions of H_2O and $[XeF][AsF_6]$, as well as HF and BrF_5 solutions of XeF_2 and $[H_3O][AsF_6]$. Reactions of HOF with HF/AsF_5 and $HOSO_2F/SbF_5$ were also studied to establish whether HOF can be protonated in superacidic media. Solid products of the reactions of XeF_2 with H_3O^+ were studied by low-temperature Raman spectroscopy in situ under HF solvent and at various stages during controlled warm-up of solid reaction mixtures toward room temperature. Finally, reaction conditions for the reliable syntheses of $[Xe_3OF_3][PnF_6]$ (Pn = As, Sb) salts in anhydrous HF have been parametrized.

(a) $[FXeOXeFXeF][AsF_6]$. Equimolar solutions of $[XeF][AsF_6]$ and H_2O (ca. 1 M each) in HF at −78 °C were found to be in equilibrium with $[H_3O][AsF_6]$ and XeF_2 (eq 1; see NMR spectroscopy). At a higher XeF^+ concentration, trigonal $[Xe_2F_3][AsF_6]$ crystallized from a HF solution that was initially composed of $[XeF][AsF_6]$ and H_2O in a 3:1 molar ratio (ca. 2.8 M in XeF^+) at −30 °C (eq 2). When larger excesses of H_2O were used (i.e., 2:1 and 4:1 molar ratios of $H_2O/[XeF][AsF_6]$) at −30 °C, the right-hand side of eq 1 was favored. Beyond the establishment of these equilibria, the complex reactions that take place among XeF_2, $[H_3O][AsF_6]$, $[XeF][AsF_6]$, and H_2O in HF solution were extensively investigated by periodically monitoring the low-temperature Raman spectra of the resulting solid mixtures under frozen HF solvent and by single-crystal X-ray diffraction and were shown to yield three cationic xenon species, XeF^+, $Xe_2F_3^+$, and $Xe_3OF_3^+$.

$$[XeF][AsF_6] + HF + H_2O \rightleftharpoons XeF_2 + [H_3O][AsF_6] \quad (1)$$

$$[XeF][AsF_6] + XeF_2 \rightleftharpoons [Xe_2F_3][AsF_6] \quad (2)$$

(i) XeF^+/H_2O in HF at −78 °C. The $[XeF][AsF_6]/H_2O$ and $XeF_2/[H_3O][AsF_6]$ systems showed no tendency to eliminate xenon gas at −78 °C over periods of up to 8 months and were initially investigated at this temperature because the reaction rates were sufficiently slow to permit low-temperature Raman spectra of the reaction intermediates to be recorded at various intervals. Moreover, equimolar reaction mixtures of $[XeF][AsF_6]$ and H_2O were soluble in HF at initial concentrations of ca. 0.5 M and were stable with respect to Xe(II) reduction up to −30 °C, decomposing above this temperature with xenon gas evolution ($\delta(^{129}Xe)$, −5308.3 ppm; xenon dissolved in HF at −30 °C). This behavior contrasts with the original report of the oxidative fluorination of H_2O by XeF^+ at −60 °C to yield H_2OF^+ and Xe gas.[10] Reaction rates were strongly dependent on the concentration and the degree of initial mixing. Typically, at equimolar XeF^+/H_2O concentrations at −78 °C in HF, $[H_3O][AsF_6]\cdot 2XeF_2$ was initially formed within ca. 24 h at 0.25 M and within ca. 2 h at 2 M, followed by the formation of $[Xe_2F_3][AsF_6]$ as the major species in the solid precipitate within ca. 48 h at 0.25 M and within ca. 2 h at 2 M. Upon standing for 0.5−8 days at −78 °C, deep red-orange, crystalline $[Xe_3OF_3][AsF_6]$ was formed as the major product. The highest initial concentration of XeF^+/H_2O (2 M) provided the most rapid synthesis of $[Xe_3OF_3][AsF_6]$.

(ii) Intermediacy of FXeOH and H_2O---XeF^+. To account for the formation of $Xe_3OF_3^+$, the intermediate FXeOH is necessary, and it is reasonable to assume that it is initially formed by the hydrolysis of XeF_2 and/or XeF^+ (eqs 3 and 4). The FXeOH intermediate then reacts with $Xe_2F_3^+$ to form $[Xe_3OF_3][AsF_6]$ (eq 5), which is stable in HF solvent.

$$XeF_2 + H_2O \rightleftharpoons FXeOH + HF \quad (3)$$

$$XeF^+ + H_2O \rightleftharpoons H_2O\text{---}XeF^+ \rightleftharpoons FXeOH + H^+ \quad (4)$$

$$FXeOH + FXeFXeF^+ \rightarrow FXeOXeFXeF^+ + HF \quad (5)$$

To underscore the sensitivity of the synthesis of $[Xe_3OF_3][AsF_6]$ to reaction conditions and the intermediacies of FXeOH and/or H_2O---XeF^+, a dilute solution of XeF_2 (0.20 M) and $[H_3O][AsF_6]$ (0.20 M) was allowed to equilibrate at −64 °C for 12 h. Although the resulting clear, colorless solution did not show any signs of xenon evolution during this time period, $[Xe_3OF_3][AsF_6]$ also did not crystallize during this time interval. Rapid removal of the solvent at −64 °C resulted in a mixture of $[H_3O][AsF_6]\cdot 2XeF_2$, $[XeF][AsF_6]$, and $[Xe_2F_3][AsF_6]$. This behavior is in accordance with our general observation that H_3O^+ ion is quite resistant to oxidative attack by strong oxidizers and does not readily participate in hydrolysis reactions. Thus, it appears that free H_2O is needed to form FXeOH (eqs 3 and 4). Rapid removal of HF from the equilibrium mixture apparently did not allow sufficient time to establish a significant equilibrium concentration of H_2O (eq 1) that would be needed to form FXeOH and $Xe_3OF_3^+$ (eq 5).

The roles of eqs 1 and 2 are also supported by the reaction of H_2O with a 3-fold molar excess of $[XeF][AsF_6]$ in HF. Even after 7 months at −78 °C, no $Xe_3OF_3^+$ had formed. The white solid that was obtained was shown by Raman spectroscopy to be a mixture of $[Xe_2F_3][AsF_6]$, $[H_3O][AsF_6]$, and $[XeF][AsF_6]$. Single-crystal X-ray diffraction also established the presence

---

(14) Ogden, J. S.; Turner, J. J. *Chem. Commun.* **1966**, 693–694.
(15) Gillespie, R. J.; Schrobilgen, G. J. *J. Chem. Soc., Chem. Commun.* **1977**, 595–597.
(16) Brock, D. S.; Bilir, V.; Mercier, H. P. A.; Schrobilgen, G. J. *J. Am. Chem. Soc.* **2007**, *129*, 3598–3611.
(17) Smith, D. F. *Science* **1963**, *140*, 899–900.
(18) Huston, J. L.; Willett, R. D.; Peterson, S. W. *J. Chem. Phys.* **1973**, *59*, 453–459.
(19) Huston, J. L.; Claassen, H. H. *J. Chem. Phys.* **1971**, *55*, 1505–1507.
(20) Huston, J. L. *J. Am. Chem. Soc.* **1971**, *93*, 5255–5256.
(21) Gillespie, R. J.; Schrobilgen, G. J. *Inorg. Chem.* **1974**, *13*, 2370–2374.
(22) Gillespie, R. J.; Landa, B.; Schrobilgen, G. J. *Inorg. Chem.* **1976**, *15*, 1256–1263.
(23) Mercier, H. P. A.; Sanders, J. C. P.; Schrobilgen, G. J.; Tsai, S. S. *Inorg. Chem.* **1993**, *32*, 386–393.
(24) Christe, K. O.; Wilson, W. W. *Inorg. Chem.* **1988**, *27*, 2714–2718.
(25) Pointner, B. E.; Suontamo, R. J.; Schrobilgen, G. J. *Inorg. Chem.* **2006**, *45*, 1517–1534.
(26) Holloway, J. H. *J. Fluorine Chem.* **1986**, *33*, 149–157.

of $[Xe_2F_3][AsF_6]$ in its trigonal modification.[27] The formation of $[Xe_3OF_3][AsF_6]$ was apparently prevented because H_2O is suppressed and $Xe_2F_3^+$ and H_3O^+ formation are favored by eq 1 and 2 at high XeF^+ concentrations.

(b) Optimized Syntheses of $[Xe_3OF_3][PnF_6]$ (Pn = As, Sb). The most efficient syntheses of high-purity $[Xe_3OF_3][PnF_6]$ involved dissolution of near-equimolar amounts of $[H_3O][PnF_6]$ and XeF_2 (up to ca. 20 mol % excess XeF_2) at ca. 0.2−3 M H_3O^+ in HF at −50 °C, followed by rapid warming of the solution to −35 °C for ca. 30 s to effect dissolution of XeF_2, followed by immediate cooling to −50 °C. These reactions were shown in the prior discussion to be very slow at −78 °C but accelerated dramatically at −50 °C. After 5 min at −50 °C, a deep red-orange voluminous precipitate of $[Xe_3OF_3][PnF_6]$ formed. Maintenance of the reaction mixture at −50 °C for an additional 20−30 min ensured that the equilibrium had been established. Unreacted XeF_2 and $[H_3O][PnF_6]$, as well as any $[Xe_2F_3][PnF_6]$ byproduct, were soluble and were decanted from the precipitate at −50 °C. Although the amount of XeF_2 relative to $[H_3O][PnF_6]$ was significantly less than the ideal 3:1 stoichiometric ratio required by the overall reaction (eq 6), the 1:1 stoichiometry provided, through equilibrium 1, for the simultaneous presence of XeF_2 and H_2O that is required for FXeOH formation. Decanting of the supernatant from the precipitated product at −50 °C ensured that the product was relatively free of unreacted starting materials and $[Xe_2F_3][PnF_6]$. Above −30 °C, $[Xe_3OF_3][PnF_6]$ decomposed under HF with Xe gas evolution, as confirmed by ^{129}Xe NMR spectroscopy (vide supra).

$$3XeF_2 + [H_3O][PnF_6] \rightarrow [Xe_3OF_3][PnF_6] + 3HF \qquad (6)$$

(c) $[H_3O][AsF_6]\cdot 2XeF_2$. Hydrogen-bond formation between the F-ligands of XeF_2 and $[H_3O][AsF_6]$ yields $[H_3O][AsF_6]\cdot 2XeF_2$ (eq 7). The adduct was isolated from HF solution between −78 °C and the freezing point of HF as colorless to very pale orange crystals (see X-ray Crystallography).

$$[H_3O][AsF_6] + 2XeF_2 \rightarrow [H_3O][AsF_6]\cdot 2XeF_2 \qquad (7)$$

When HF-free solid $[H_3O][AsF_6]\cdot 2XeF_2$ was allowed to warm toward room temperature for very brief time periods, followed by quenching to −130 °C, the composition progressively shifted toward XeF^+/H_2O, in accord with equilibrium 1. Warming $[H_3O][AsF_6]\cdot 2XeF_2$ for longer time periods to room temperature resulted in a transient red-orange solid, presumably $[Xe_3OF_3][AsF_6]$, which rapidly melted with Xe, O_2, and HF evolution, leaving behind residues of $[XeF][AsF_6]$ and $[H_3O][AsF_6]$. When solid $[H_3O][AsF_6]\cdot 2XeF_2$ was allowed to decompose in a sealed glass tube and the decomposition products were cooled to −78 °C or below, an intense blue-green product was obtained that was attributed to the reversible formation of $[Xe_2][AsF_6]$ from Xe and $[XeF][AsF_6]$ (eq 8).[28]

$$3[XeF][AsF_6] + 3Xe \rightleftharpoons [Xe_2F_3][AsF_6] + 2[Xe_2][AsF_6] \qquad (8)$$

(d) XeF_4/H_3O^+ System and Formation of $[FXeOXeFXeF][SbF_6]$. In the pursuit of other novel xenon oxide fluorides, the reaction of XeF_4 with $[H_3O][SbF_6]$ in HF was explored as a possible route to the $OXeF^+$ cation (eqs 9−11). Instead, Raman spectroscopy showed the formation of $[XeF][SbF_6]$, $[Xe_2F_3][SbF_6]$, and $[Xe_3OF_3][SbF_6]$; the latter salt was also characterized by a crystal structure determination (see X-ray Crystallography). The $[XeF][SbF_6]$ salt is likely formed by oxygen loss from an unstable $OXeF^+$ intermediate (eq 12) which, in turn, reacts with H_2O in HF to generate $[Xe_2F_3][SbF_6]$ and $[Xe_3OF_3][SbF_6]$ (eqs 1−5).

Table 1. Calculated and Experimental ^{1}H and ^{19}F Chemical Shifts for H_2OF^+, HOF, $H_2NF_2^+$, and HNF_2

			chemical shifts, ppm[a]			
			δ(^{1}H)		δ(^{19}F)	
compd	solvent	temp, °C	exptl	calcd	exptl	calcd
HOF	CCl_4/CD_2Cl_2[b]	25	12.8	11.9	27.5	33.5
	CH_3CN[c]	25	15.5		−8.5	
	SO_2ClF[d]	−70	12.9		16.0	
	AsF_5/HF	−70	*e*		*e*	
	$SbF_5/HOSO_2F$	−70	*e*		*e*	
H_2OF^+	HF	−60	(8.06)[f]	11.1	(−68.0)[f]	359.2
HNF_2	*g*	*g*	7.2[h]	10.2	−6.0[h]	−11.7
$H_2NF_2^+$	HF	−40	14.2[h]	10.7	11.6[h]	16.8

[a] Chemical shifts were calculated by the GIAO-MBP2 method using CCSD(T)/aug-cc-pVDZ optimized geometries. The calculated ^{1}H and ^{19}F chemical shifts were obtained by subtracting the calculated isotropic chemical shift from the calculated isotropic chemical shifts of TMS and $CFCl_3$, respectively. [b] 5:1 v/v.[9] [c] Reference 9. [d] This work. [e] This work; neither HOF nor H_2OF^+ were observed, most as a result of ^{1}H and/or ^{19}F exchange between HOF and $HF/HOSO_2F$. [f] Incorrect values reported in ref 10. [g] No solvent or temperature were provided in the original work (ref 30). The ^{1}H and ^{19}F chemical shifts reported in ref 30 were recalculated and referenced to $CFCl_3$ in ref 31. [h] Reported in ref 31.

$$[H_3O][SbF_6] + XeF_4 \rightleftharpoons H_2O + [XeF_3][SbF_6] + HF \qquad (9)$$

$$XeF_3^+ + H_2O \rightleftharpoons H_2O\cdots XeF_3^+ \rightleftharpoons F_2XeOH^+ + HF \qquad (10)$$

$$F_2XeOH^+ \rightarrow OXeF^+ + HF \qquad (11)$$

$$[OXeF][SbF_6] \rightarrow [XeF][SbF_6] + {}^1/_2O_2 \qquad (12)$$

(e) NMR Spectroscopy. (i) Attempted Protonation of HOF. A sample of HOF was prepared by the literature method,[29] and its ^{1}H and ^{19}F NMR spectra were recorded in SO_2ClF solution at −60 °C. The ^{19}F (16.0 ppm, $^2J(^{19}F-^1H)$ = 73 Hz) and ^{1}H (12.9 ppm, $^2J(^1H-^{19}F)$ = 73 Hz) NMR parameters were in close agreement with the published values (27.5, 12.8 ppm; 80−83 Hz, respectively) in 5:1 CCl_4/CD_2Cl_2 solvent (Table 1). Addition of a 3-fold molar excess of a 1:1 mixture of either AsF_5/HF or $SbF_5/HOSO_2F$ to SO_2ClF solutions of HOF did not provide any evidence for the formation of H_2OF^+ by way of significant chemical shift or coupling constant changes (see Computational Results).

(ii) Reaction of $[XeF][AsF_6]$ with H_2O in HF. Equimolar mixtures of $[XeF][AsF_6]$ and H_2O (ca. 1 M each) in HF solution at −78 °C were found to slowly react to form $[H_3O][AsF_6]$ and XeF_2 (eq 1). Xenon difluoride was identified at −75 °C by ^{19}F and ^{129}Xe NMR spectroscopy (δ(^{129}Xe), −1516.3 ppm; δ(^{19}F), −200.68 ppm, $^1J(^{129}Xe-^{19}F)$, 5670 Hz). In addition to the XeF_2 and the HF solvent resonances (−193.66 ppm; $\Delta\nu_{1/2}$, 38 Hz), a broad singlet at −68.5 ppm ($\Delta\nu_{1/2}$, 1560 Hz) corresponding to the AsF_6^- anion was observed in the ^{19}F NMR spectrum. The

---

(27) Fir, B. A.; Gerken, M.; Pointner, B. E.; Mercier, H. P. A.; Dixon, D. A.; Schrobilgen, G. J. *J. Fluorine Chem.* **2000**, *105*, 159–167.

(28) Stein, L.; Norris, J. R.; Downs, A. J.; Minihan, A. R. *J. Chem. Soc., Chem. Commun.* **1978**, 502–504.

(29) Appelman, E. H.; Jache, A. W. *J. Am. Chem. Soc.* **1987**, *109*, 1754–1757.

(30) Kennedy, A.; Colburn, C. B. *J. Am. Chem. Soc.* **1959**, *81*, 2906–2907.

(31) Christe, K. O. *Inorg. Chem.* **1975**, *14*, 2821–2824.

^{17}O NMR spectrum of a sample prepared from ^{17}O-enriched H_2O (^{16}O, 35.4%; ^{17}O, 21.9%; ^{18}O, 42.7%) showed a singlet at −0.47 ppm ($\Delta\nu_{1/2}$, 177 Hz), which is assigned to H_3O^+ ($\delta(^{17}O)$, 10.2 ppm; SO_2 solvent at −20 °C)[32] and was broad, owing to exchange with HF and residual H_2O, preventing the observation of the $^1J(^{17}O-^1H)$ coupling (103.5 Hz).[32]

(iii) Reactions of XeF_2 with $[H_3O][AsF_6]$ in BrF_5 Solution. In an attempt to observe either FXeOH or $Xe_3OF_3^+$ by solution ^{19}F NMR spectroscopy and to circumvent possible rapid chemical exchange with the solvent, XeF_2 was allowed to react with $[H_3O][AsF_6]$ in BrF_5 at −55 °C. The initial ^{19}F NMR spectrum of a sample of XeF_2 and $[H_3O][AsF_6]$ in BrF_5 consisted of resonances corresponding to XeF_2 (−183.25 ppm; $^1J(^{129}Xe-^{19}F) = 5737$ Hz), AsF_6^- (−59.71 ppm), and BrF_5 (F_{ax}, 273.22 ppm; F_{eq}, 135.73 ppm; $^2J(^{19}F-^{19}F) = 76$ Hz). After several minutes at −55 °C, resonances corresponding to $Xe_2F_3^+$ (F_t, −250.05 ppm, F_b, −183.48 ppm; $^2J(^{19}F-^{19}F) = 299$ Hz, $^1J(^{129}Xe-^{19}F_t) = 6659$ Hz; ^{129}Xe satellites of F_b overlapped with the resonances of XeF_2 and HF), HF (−192.33 ppm; $^1J(^{19}F-^1H) = 519$ Hz), and BrO_2F (194.35 ppm, $\Delta\nu_{1/2} = 1950$ Hz) were also observed and increased with time relative to the ^{19}F resonance of XeF_2. Equation 13 accounts for the resonances observed in the NMR spectra. In contrast to the analogous reaction in HF, where excess HF shifts eq 1 completely to the side of XeF_2 and H_3O^+, XeF_2 and H_3O^+ are partially converted to XeF^+, H_2O, and HF. The interaction of XeF_2 and XeF^+ subsequently yields the $Xe_2F_3^+$ cation, and H_2O reacts with BrF_5 solvent to form BrO_2F and HF. The ^{19}F NMR signals for HF and $Xe_2F_3^+$ broadened with time, presumably because intermolecular exchange between HF and $Xe_2F_3^+$ increases with increasing concentration.

$$2XeF_2 + 2[H_3O][AsF_6] + BrF_5 \xrightarrow{BrF_5} [Xe_2F_3][AsF_6] + BrO_2F + 6HF \quad (13)$$

(f) Reaction of XeF^+/H_2O with ClF_3 in HF Solvent. The prior claim[10,11] that solutions of $[XeF][AsF_6]$ and H_2O in HF oxygenate ClF_3 to $ClOF_2^+$ was re-examined. Under nearly identical experimental conditions, an equimolar solution of $[XeF][AsF_6]$ and H_2O in HF solvent was initially allowed to react at −64 °C for 12 h, followed by the addition of an equimolar amount of ClF_3 at −196 °C. Warming of the reaction mixture for 2 min to −78 °C yielded a red suspension that subsequently turned white. In contrast with the earlier claim that $ClOF_2^+$ was formed, only $[ClO_2][AsF_6]$ was isolated. The present findings are reminiscent of the reaction of H_2O with $[ClF_2][AsF_6]$ in HF at −78 °C,[33] in which a red-brown color was initially observed and $[ClO_2][AsF_6]$ and unreacted $[ClF_2][AsF_6]$ were recovered. The formation of $[ClO_2][AsF_6]$ in the XeF^+/H_2O system is not surprising because ClF_3 is known to hydrolyze rapidly to unstable FClO, which dismutates to ClF and $FClO_2$. In the presence of AsF_5, $FClO_2$ forms stable $[ClO_2][AsF_6]$, while the thermally unstable $[Cl_2F][AsF_6]$ byproduct (dissociation vapor pressure ca. 4864 Torr at 25 °C)[34] was pumped away under the given conditions.

(g) Overview of the XeF^+/H_2O and XeF_2/H_3O^+ Systems and Their Reactions. In the present work, neither the previously reported syntheses of $[H_2OF][PnF_6]$ salts from the reactions of H_2O with $[XeF][PnF_6]$ in anhydrous HF nor the alleged oxidative oxygenating reactions of such solutions toward ClF_3[10,11] could be duplicated. Rather, the XeF^+/H_2O and XeF_2/H_3O^+ systems were demonstrated to be very complex and to involve, as a minimum, the reactions shown in Scheme 1. The crystal structures of $[H_3O][AsF_6]\cdot 2XeF_2$ and $[FXeOXeFXeF][PnF_6]$ (see X-ray Crystallography) have been key to understanding the true nature of the XeF^+/H_2O and XeF_2/H_3O^+ systems.

Scheme 1. Products Resulting from the Equilibrium between XeF^+/H_2O and XeF_2/H_3O^+ (Pn = As, Sb)

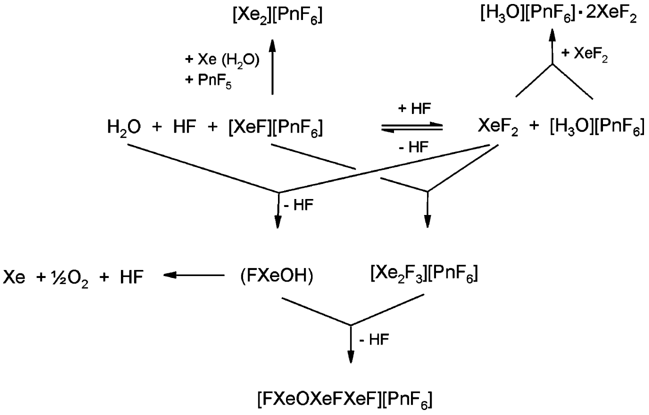

In HF solution, mixtures of XeF^+ and H_2O were shown to quickly establish an equilibrium with XeF_2 and H_3O^+. This equilibrium was strongly influenced by the amount of HF present. With a large excess of HF, the equilibrium is shifted completely to the side of XeF_2 and H_3O^+. Hydrogen fluoride plays a 2-fold role in influencing this equilibrium. There is the obvious mass effect expected from the Le Chatelier Principle; however, the main driving force is the vastly different acidities of monomeric and polymeric HF. Polymeric HF has been shown to be a much stronger acid than monomeric HF.[35] Therefore, $[H_3O][HF_2\cdot nHF]$ can displace XeF_2 from its XeF^+ salts, while XeF_2 can displace monomeric HF from its H_3O^+ salts. This phenomenon has been previously observed in azide systems, where polymeric, liquid HF can quantitatively displace HN_3 from ionic azides, while HN_3 can displace monomeric HF from solid ionic fluoride salts.[35] Reactions of both $[XeF][PnF_6]$ with H_2O, and XeF_2 with $[H_3O][PnF_6]$ in HF solution demonstrated that the reaction proposed in Scheme 1 is a true equilibrium, as it was established from both sides.

The formation of $Xe_2F_3^+$ from XeF^+ and XeF_2 is well-known.[27,36] The co-crystallization of $[H_3O][AsF_6]$ and XeF_2 as the hydrogen-bonded adduct, $[H_3O][AsF_6]\cdot 2XeF_2$, is not surprising, because XeF_2 is known to form hydrogen bonds with the strong acid, HNO_3.[37]

The remaining products identified in the XeF^+/H_2O system stem from the components of the equilibrium reacting with each other, as summarized in Scheme 1. The only component of Scheme 1 that was not directly observed was FXeOH. Its formation as an intermediate, however, accounts for the formation of the catenated $FXeOXeFXeF^+$ cation according to eq 5,

---

(32) Olah, G. A.; Berrier, A. L.; Prakash, G. K. S. *J. Am. Chem. Soc.* **1982**, *104*, 2373–2376.
(33) Christe, K. O. *Inorg. Chem.* **1972**, *11*, 1220–1222.
(34) Christe, K. O.; Sawodny, W. *Inorg. Chem.* **1969**, *8*, 212–219.
(35) Christe, K. O.; Wilson, W. W.; Bau, R.; Bunte, S. W. *J. Am. Chem. Soc.* **1992**, *114*, 3411–3414.
(36) Sladky, F.; Bulliner, P. A.; Bartlett, N. *J. Chem. Soc. A.* **1969**, *14*, 2179–2188.
(37) Moran, M. D. Ph.D. Thesis, McMaster University, Hamilton, Ontario, Canada, 2007.

Table 2. Summary of Crystal Data and Refinement Results for $[Xe_3OF_3][PnF_6]$ (Pn = As, Sb) and $[H_3O][AsF_6]\cdot 2XeF_2$

	$[Xe_3OF_3][AsF_6]$	$[Xe_3OF_3][SbF_6]$	$[H_3O][AsF_6]\cdot 2XeF_2$
space group	*Pc* (No. 13)	$P2_1/c$ (No. 14)	*I4/mcm* (No. 140)
chemical formula	F_9OAsXe_3	F_9OSbXe_3	$H_3F_{10}OAsXe_2$
a (Å)	6.711(1)	6.687(1)	8.714(4)
b (Å)	9.115(2)	9.306(2)	8.714(4)
c (Å)	8.674(2)	8.822(2)	12.988(9)
β (deg)	96.85(3)	96.784(5)	90
V (Å^3)	526.8(2)	545.1(2)	986.4(9)
Z (molecules/unit cell)	2	2	4
mol wt (g mol^{-1})	655.82	702.65	546.54
calcd density (g cm^{-3})	4.135	4.281	3.680
T (°C)	−116	−125	−173
μ (mm^{-1})	12.81	11.790	10.32
λ (Å)	0.71073	0.71073	0.71073
R_1[a]	0.0460	0.0419	0.0208
wR_2[b]	0.1311	0.0896	0.0544

[a] R_1 is defined as $\Sigma||F_o| - |F_c||/\Sigma|F_o|$ for $I > 2\sigma(I)$. [b] wR_2 is defined as $[\Sigma[w(F_o^2 - F_c^2)^2]/\Sigma w(F_o^2)^2]^{1/2}$ for $I > 2\sigma(I)$.

which can arise through either partial hydrolysis of XeF_2 (eq 3) or deprotonation of the XeF^+/H_2O donor−acceptor adduct (eq 4) as the first step in this sequence of reactions. The fact that FXeOH was not directly observed is not surprising, because compounds containing OH and F ligands attached to the same central atom are highly reactive and can undergo very facile intramolecular HF elimination.[38]

The formation of the $FXeOXeFXeF^+$ cation, the red-orange species erroneously attributed to H_2OF^+,[10,11] was unforeseen. It constitutes the first oxide fluoride of Xe(II) and, along with $[H_3O][AsF_6]\cdot 2XeF_2$, forms the basis for much of the remaining structural and theoretical discussion.

X-ray Crystallography. Details of the data collection parameters and other crystallographic information for $[Xe_3OF_3][PnF_6]$ (Pn = As, Sb) and $[H_3O][AsF_6]\cdot 2XeF_2$ are given in Table 2. Experimental and calculated bond lengths and angles in $[Xe_3OF_3][PnF_6]$ are provided in Table 3.

(a) $[Xe_3OF_3][PnF_6]$, (Pn = As, Sb). Single-crystal X-ray diffraction revealed that the As and Sb salts of $[Xe_3OF_3][PnF_6]$ crystallize in the monoclinic space groups *Pc* and $P2_1/c$, respectively. Both structures consisted of well-separated but positionally disordered $Xe_3OF_3^+$ cations and PnF_6^- anions (Figure 1a). The experimental and calculated (SVWN/aug-cc-pVTZ(-PP)) geometries of the $Xe_3OF_3^+$ cation (also see Computational Results) are depicted in Figure 1b and show generally good agreement. The PnF_6^- anions are packed in chains along the *a*-axis and are located in channels that are formed by the $Xe_3OF_3^+$ cations (Figures S1 and S2, Supporting Information). Substitution of the AsF_6^- anion with SbF_6^- results in widening of the anion channels and significant increases in the lengths of the *b*- and *c*-axes. Because the packing along the *a*-axis in both $[Xe_3OF_3][PnF_6]$ salts is dominated by the cations, the observation of a shorter *a*-axis in $[Xe_3OF_3][SbF_6]$ is most likely a thermal effect because the data for the SbF_6^- salt were acquired at a lower temperature.

Table 3. Experimental Geometrical Parameters for the $Xe_3OF_3^+$ Cation in $[Xe_3OF_3][PnF_6]$ (Pn = As, Sb) and Calculated Geometrical Parameters for the $Xe_3OF_3^+$ Cation

AsF_6^- salt[a,b]		SbF_6^- salt[b,c]	
bond lengths (Å)			
Xe(1)−F(1)	1.992(6)	Xe(1)−F(1)	1.975(6)
Xe(1)−O/F(1)	2.101(10)	Xe(1)−O/F(2)	2.085(6)
Xe(2)−O/F(1)	1.919(9)	Xe(2)−O/F(2)	1.908(6)
Xe(2)---F/O(2)	2.502(10)	Xe(2)---F/O(2A)	2.513(6)
Xe(3)−F/O(2)	2.104(9)	Xe(1A)−F/O(2A)	2.085(6)
Xe(3)−F(3)	1.977(6)	Xe(1A)−F(1A)	1.975(6)
bond angles (deg)			
F(1)−Xe(1)−O/F(1)	177.4(5)	F(1)−Xe(1)−O/F(2)	178.6(3)
Xe(1)−O/F(1)−Xe(2)	123.5(6)	Xe(1)−O/F(2)−Xe(2)	124.6(3)
O/F(1)−Xe(2)---F/O(2)	178.3(5)	O/F(2)−Xe(2)---F/O(2A)	177.9(1)
Xe(2)---F/O(2)−Xe(3)	123.6(6)	Xe(2)---F/O(2A)−Xe(1A)	124.6(3)
F/O(2)−Xe(3)−F(3)	178.2(5)	F/O(2A)−Xe(1A)−F(1A)	178.6(3)

	calcd[d]					
	SVWN	BP86	PBE1PBE	B3LYP	B3PW91	MP2
bond lengths (Å)						
Xe_1-F_1	1.965	2.004	1.948	1.974	1.960	1.958
Xe_1-O_1	2.139	2.198	2.158	2.189	2.169	2.151
O_1-Xe_2	1.972	2.014	1.955	1.984	1.968	1.952
Xe_2---F_2	2.316	2.414	2.405	2.440	2.418	2.378
F_2-Xe_3	2.119	2.156	2.108	2.133	2.118	2.111
Xe_3-F_3	1.931	1.971	1.926	1.950	1.936	1.925
bond angles (deg)						
$F_1-Xe_1-O_1$	175.2	174.5	175.8	175.3	175.5	176.5
$Xe_1-O_1-Xe_2$	119.3	120.4	120.8	121.7	121.2	117.1
O_1-Xe_2---F_2	179.6	174.0	177.6	177.4	177.1	177.1
Xe_2---F_2-Xe_3	151.4	160.9	170.0	171.6	179.9	177.2
$F_2-Xe_3-F_3$	178.8	179.0	179.7	179.7	179.8	179.9

[a] The As−F distances and F−As−F angles range from 1.64(2) to 1.89(2) Å and 85.8(8)° to 109.2(9)°, respectively. [b] The complete list of bond lengths and bond angles can be found in Supporting Information (cif files). [c] The Sb−F distances and F−Sb−F angles range from 1.846(14) to 1.904(11) Å and 87.5(6)° to 91.6(5)°, respectively. [d] aug-cc-pVTZ(-PP).

The $Xe_3OF_3^+$ cations in both PnF_6^- salts are disordered but must contain three xenon atoms, two terminal fluorine atoms, one bridging fluorine atom, and one bridging oxygen atom. The presence of an oxygen atom in the cation is unambiguously established by the observed ^{18}O isotopic shifts in the vibrational spectra and quantum-chemical calculations (see Raman Spectroscopy and Computational Results). The bridging oxygen and fluorine positions are disordered, which causes the bridging Xe(2) position to be split between a longer Xe(2)---F/O and a shorter Xe(2)−O/F bond. In the case of the SbF_6^- salt, the disorder results from a crystallographic inversion center, whereas in the AsF_6^- salt, the bridging Xe(2) and Xe(2A) atoms are situated on two crystallographically independent sites. Attempts to resolve the O/F positions into two components were unsuccessful. Because the O/F occupancy factors are 50/50, extrapolation methods[39,40] could not be applied to extract the individual Xe−O/F bond lengths from these data sets. Thus, quantum-chemical calculations were relied upon to obtain remaining structural details (see Computational Results). The two bonding models, (a) $FXeOXe^+$---FXeF and (b) $FXeFXe^{2+}$---$OXeF^-$, are not distinguishable solely on the basis of diffraction data. However, model a, which can be rationalized as the addition of XeF_2 to a $FXeOXe^+$ fragment, was chosen because model b would result in an unfavorable charge distribution giving rise to negatively and double positively charged fragments. The $Xe_3OF_3^+$ cation is nearly planar with a mean deviation from the molecular plane of ± 0.017 Å. Quantum-chemical calculations confirmed the assignment to model a, as well as the near-planarity of the cation (mean deviation, ±0.012 Å; see Computational Results).

---

(38) Christe, K. O.; Hegge, J.; Hoge, B.; Haiges, R. *Angew. Chem., Int. Ed.* **2007**, *46*, 6155–6158.

(39) Vij, A.; Zhang, X.; Christe, K. O. *Inorg. Chem.* **2001**, *40*, 416–417.

(40) Lork, E.; Mews, R.; Viets, D.; Watson, P. G.; Borrmann, H.; Vij, A.; Boatz, J. A.; Christe, K. O. *Inorg. Chem.* **2001**, *40*, 1303–1311.

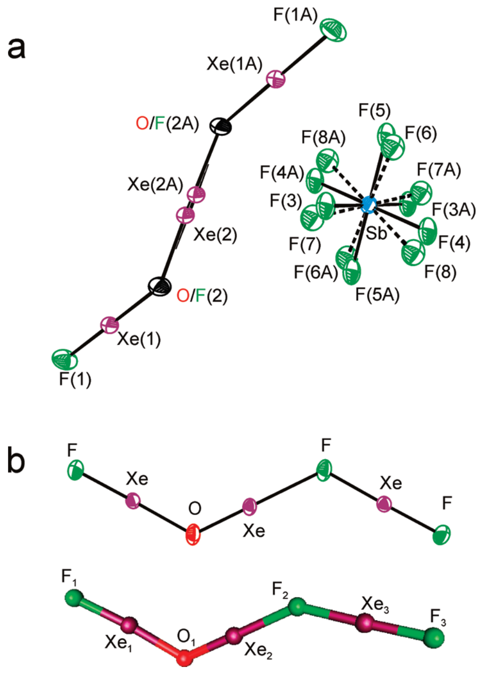

Figure 1. (a) Disordered structure of $[Xe_3OF_3][SbF_6]$. Thermal ellipsoids are given at the 50% probability level. (b) One of the two orientations obtained from the experimental crystal structure, and the calculated geometry (SVWN/aug-cc-pVTZ(-PP)) for the $Xe_3OF_3^+$ cation.

The only bond lengths that are unaffected by the disorder are those of the terminal Xe−F bonds [As, 1.977(6) and 1.992(6) Å; Sb, 1.975(6) Å], which are comparable to the Xe−F bond length in XeF_2 (2.00(1) Å)[41] and are longer than the terminal Xe−F bonds in $Xe_2F_3^+$ (1.929(6) Å, 1.908(7), and 1.908(6) Å).[27] The bond angle around the xenon atom also is not affected by the disorder, with the F−Xe−O/F angles [As, 177.4(5)° and 178.2(5)°; Sb, 178.6(3)°] deviating only slightly from linearity.

The PnF_6^- anions are disordered between two orientations and exhibit Xe---F contacts to the $Xe_3OF_3^+$ cation that are as short as 3.021−3.114 Å (As) and 2.980−3.087 Å (Sb), which are significantly less than the sum of the van der Waals radii of xenon and fluorine (3.63 Å).[42]

(b) $[H_3O][AsF_6]\cdot 2XeF_2$. The compound $[H_3O][AsF_6]\cdot 2XeF_2$ crystallizes in the tetragonal space group *I*4/*mcm* and consists of two XeF_2 molecules, one H_3O^+ cation, and one AsF_6^- anion (Figure 2). The oxygen atom of the H_3O^+ cation is located on a high-symmetry position (*m.mm*), which precludes the observation of the hydrogen atoms in the electron density difference map. The xenon atom of XeF_2 is also located on a high-symmetry position (*..2/m*), giving two equivalent fluorine atoms, preventing the observation of the asymmetry of XeF_2 as made evident by Raman spectroscopy (vide infra). The average Xe(1)−F(3) bond length of 1.984(3) Å is similar to that found in the crystal structures of XeF_2 (2.00(1) Å)[41] and $XeF_2\cdot N_2O_4$ (1.985(3) Å).[37]

The H_3O^+ cations and AsF_6^- anions pack in separate chains parallel to the *c*-axis and alternating along the *a*- and *b*-axes (Figure 2). The H_3O^+ cation exhibits four short F(3)---O(1) (2.571(3) Å) contacts to fluorine atoms belonging to four crystallographically related XeF_2 molecules, which indicate the presence of hydrogen bonding between XeF_2 and H_3O^+. The F(3)---O(1) distance is shorter than the F---O distance determined for $XeF_2\cdot HNO_3$ (2.690(1) Å),[37] in agreement with the higher positive charge on H_3O^+, and is within the sum of the van der Waals radii for O and F (2.99 Å).[42]

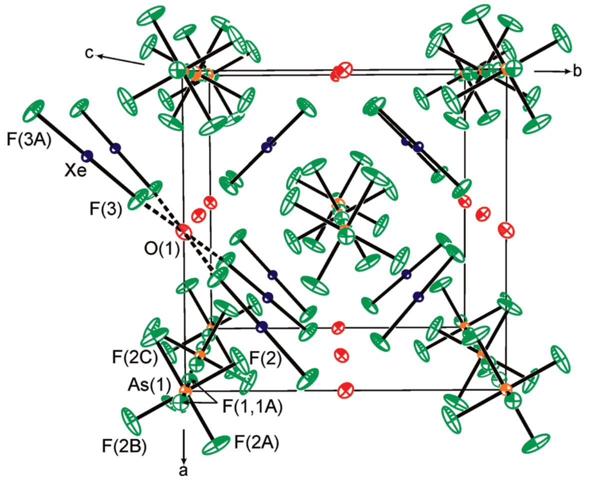

Figure 2. Packing diagram of $[H_3O][AsF_6]\cdot 2XeF_2$ along the *c*-axis showing four O···F contacts. Thermal ellipsoids given at the 50% probability level.

The AsF_6^- anions are located on special positions (4/*m*). The thermal ellipsoid of F(2) in the AsF_6^- anion is elongated in the *a*,*b*-plane, indicating some residual rotational motion along the coincident F(1)−As(1)−F(1A)- and *c*-axes. The AsF_6^- anion exhibits a tetragonal distortion from octahedral symmetry with the As(1)−F(1) bond (1.722(3) Å) longer than the As(1)−F(2) bond (1.695(3) Å). While this result is in agreement with the lowering of the anion symmetry observed by Raman spectroscopy, the local symmetry of the anion (D_{4h}) is overestimated as a result of the high crystal symmetry (D_{4h}) and, like XeF_2, shows vibrational bands consistent with a lower symmetry (vide infra).

Raman Spectroscopy. (a) $[Xe_3OF_3][PnF_6]$ (Pn = As, Sb). The Raman spectra of solid $[Xe_3{}^{16,18}OF_3][AsF_6]$ and $[Xe_3{}^{16}OF_3][SbF_6]$ were recorded at ca. −160 °C. The Raman frequencies and intensities along with their assignments are provided in Table 4. The natural abundance and ^{18}O-enriched spectra of $[Xe_3OF_3][AsF_6]$ are given in Figure 3, and the natural abundance spectrum of $[Xe_3OF_3][SbF_6]$ is given in Figure 4.

Assuming C_s symmetry for the free $Xe_3OF_3^+$ cation (see X-ray Crystallography and Computational Results), a maximum of 15 Raman- and infrared-active bands (11A′ + 4A″) are expected. The Raman spectra of the AsF_6^- and SbF_6^- salts, however, reveal 19 (natural abundance AsF_6^- salt), 21 (^{18}O-enriched AsF_6^- salt), and 19 (natural abundance SbF_6^- salt) bands that can be attributed to the $Xe_3OF_3^+$ cation (Table 4). The remaining 16 bands were assigned to the AsF_6^- anion in the spectra of the ^{16}O and ^{18}O isotopomers, whereas five bands were assigned to the SbF_6^- anion in the natural abundance salt. Overlaps between cation and AsF_6^- bands were evident from changes in the relative intensities of these bands in the spectra of the ^{16}O- and ^{18}O-substituted salts.

Factor-group analyses were carried out for the $Xe_3OF_3^+$ cation, and the AsF_6^- and SbF_6^- anions (symmetries and number of bands for the SbF_6^- salt appear in square brackets when they differ from that of the AsF_6^- salt). The factor-group analyses correlating the free cation (C_s) and anion (O_h) symmetries to their crystal site symmetries (C_1) [C_i] and to the unit cell

---

(41) Argon, P. A.; Begun, G. M.; Levy, H. A.; Mason, A. A.; Jones, C. G.; Smith, D. F. *Science* **1963**, *139*, 842–844.
(42) Bondi, A. *J. Phys. Chem.* **1964**, *68*, 441–451.

Table 4. Experimental Raman Vibrational Frequencies and Intensities for the $Xe_3OF_3^+$ Cation in $[Xe_3OF_3][AsF_6]$, $[Xe_3{}^{18}OF_3][AsF_6]$, and $[Xe_3OF_3][SbF_6]$ and Calculated Vibrational Assignments for $Xe_3OF_3^+$

$Xe_3OF_3^+$ in $[Xe_3OF_3][PnF_6]$ [a]				$Xe_3OF_3^+$
Pn = As [b]			Pn = Sb [c]	
^{16}O	^{18}O	Δν	^{16}O	assgnt [d]
595.8(44) [e]	568.8(33)	–27.0	595 sh	$\nu(Xe_1\text{-}O_1) - \nu(Xe_2\text{-}O_1)$
	564.4(37)	–31.4	593(52)	
555.7(69)	553.7(70)	–2.0	552(83)	$\nu(Xe_3\text{-}F_3) +$ $[\nu(Xe_1\text{-}O_1) - \nu(Xe_2\text{-}O_1)]_{small}$
539.5(72)	539.4(73)	0.1	537(83)	
511.9(20)	511.2(21)	–0.7	509(27)	$\nu(Xe_1\text{-}F_1)$
479.5(100)	479.1(100)	–0.4	480(100)	$[\nu(Xe_3\text{-}F_2) - \nu(Xe_2\text{-}F_2)] +$ $[\nu(Xe_1\text{-}O_1) + \nu(Xe_2\text{-}O_1)]$
429.8(48) [e]	402 sh [e]	–27.8	425 sh	$[\nu(Xe_1\text{-}O_1) + \nu(Xe_2\text{-}O_1)] +$ $[\nu(Xe_2\text{-}F_2) - \nu(Xe_3\text{-}F_2)]$
	396.2 sh		417(99) br	
418.7(63)	393.9(54) [e]	–24.8		
261(5)	261(5)	0.0	253(9)	$\delta(F_2Xe_3F_3)_{ip}$
251.9(7)	252.3(7)	0.4	248(10)	
214.4(3)	208.1(3)	–6.3	209(3)	$\delta(F_2Xe_3F_3)_{oop} + \delta(F_1Xe_1O_1)_{oop}$
206.3(3)	200.9(4)	–5.4	201(4)	
190.2 sh	190.1 sh	–0.1	185(25)	$\delta(F_2Xe_3F_3)_{oop} - \delta(F_1Xe_1O_1)_{oop}$
185.6(25)	185.6(25)	0.0	181 sh	
156.8(27)	156.4(27)	–0.4	151(37)	$\delta(F_1Xe_1O_1)_{ip}$
139.2(18)	138.9(19)	–0.3	137(22)	$\rho_r(F_1Xe_1O_1)_{ip} + \nu(Xe_2\text{-}F_2)$
123.2 br	124.7 br	0.5	121(25)	
n.o.	n.o.		n.o.	$\rho_t(F_1Xe_1O_1)_{oop} - \rho_t(F_2Xe_3F_3)_{oop}$
101.3(20)	100.5(20)	–0.8	95(18)	$\delta(Xe_2O_1Xe_1)_{ip} - \rho_r(F_2Xe_3F_3)_{ip}$
76.2(8)	76.0(8)	–0.2	73(12)	lattice modes
63.1(9)	63.2(9)	0.1		
n.o.	n.o.		n.o.	$\delta(Xe_2O_1Xe_1)_{ip} + \rho_r(F_2Xe_3F_3)_{ip}$
n.o.	n.o.		n.o.	$\rho_t(F_1Xe_1O_1Xe_2)_{oop} - \rho_t(F_2Xe_3F_3)_{oop}$
n.o.	n.o.		n.o.	$\rho_r(F_1Xe_1O_1Xe_2)_{ip} - \rho_r(F_2Xe_3F_3)_{ip}$

AsF_6^- in $[Xe_3OF_3][AsF_6]$			SbF_6^- in $[Xe_3OF_3][SbF_6]$	
$[Xe_3{}^{16}OF_3][AsF_6]$ –160 °C	$[Xe_3{}^{18}OF_3][AsF_6]$ –164.5 °C	AsF_6^- (O_h) [f]	$[Xe_3OF_3][SbF_6]$ –160 °C	SbF_6^- (O_h)
709 br	709 br	$\nu_3(T_{1u})$	n.o.	$\nu_3(T_{1u})$
681 (55)	681 (58)	$\nu_1(A_{1g})$	651 (56)	$\nu_1(A_{1g})$
596 (44) [g] 589 (13) 585 (11) 577 (12) 573 (10)	599 (15) 590 (12) 585 (11) 578 (14) 573 (15)	$\nu_2(E_g)$	581(19) 576 sh	$\nu_2(E_e)$
430 (48) [g] 402 (17) 393 (20)	429 sh 424 (45) 402 sh [g] 394 (54) [g]	$\nu_4(T_{1u})$	n.o.	$\nu_4(T_{1u})$
371 (9) 368 (6) 366 (10) 350 (2)	371 (10) 368 (7) 366 (10)	$\nu_5(T_{2g})$	281(13) [h] 278 sh	$\nu_5(T_{2g})$
244 (3) 222 (2)	244 (3) 221 (2)	$\nu_6(T_{2u})$	n.o.	$\nu_6(T_{2u})$

[a] Values in parentheses denote relative Raman intensities. Symbols denote the following: shoulder (sh), broad (br), and not observed (n.o.). [b] Some additional bands which intensity proved to vary from sample to sample were observed at 497(12) in the ^{16}O spectrum and at 503.9(19) and 544.6(31) in the ^{18}O spectrum and are tentatively assigned to XeF_2. [c] Bands arising from $[H_3O][SbF_6]$ were observed at 173(4), 281(13), 639(2), 672(6), and 681(2) cm^{-1}. An additional band arising from XeF_2 was also observed at 497(22) cm^{-1}. [d] The atom numbering scheme is as follows: $F_1{-}Xe_1{-}O{-}Xe_2{-}{-}{-}F_2{-}Xe_3{-}F_3^+$. Symbols denote stretch (ν), bend (δ), ρ_w (wag), ρ_t (twist), and ρ_r (rock). The abbreviations denote in-plane (ip) and out-of-plane (oop). Only major contributions to the mode descriptions are provided. [e] Mode coincident with a mode associated to the AsF_6^- anion. [f] Assignments are made under C_1 crystal site symmetry (see Table S1) but are correlated to O_h symmetry in this Table. [g] Mode coincident with a mode associated to the $Xe_3OF_3^+$ cation. [h] Mode coincident with a $[H_3O][SbF_6]$ mode.

symmetries (C_s) [C_{2h}] are provided in Tables S1 and S2 and show that both the cation and anion modes are split into Raman- and infrared-active A′ and A″ [Raman-active A_g and B_g, infrared-active A_u and B_u] components under C_s [C_{2h}] unit cell symmetry, giving the potential to observe a total of 60 and 34 Raman bands for the $[Xe_3OF_3][AsF_6]$ and $[Xe_3OF_3][SbF_6]$ salts, respectively, if all factor-group splittings were to be observed. Although not all of these splittings were observed, significantly more bands (35−37 and 24 bands, respectively) are observed compared to the predicted numbers of 30 and 15, respectively, if only site-symmetry lowering is operative. The additional splittings indicate that there is some vibrational coupling within

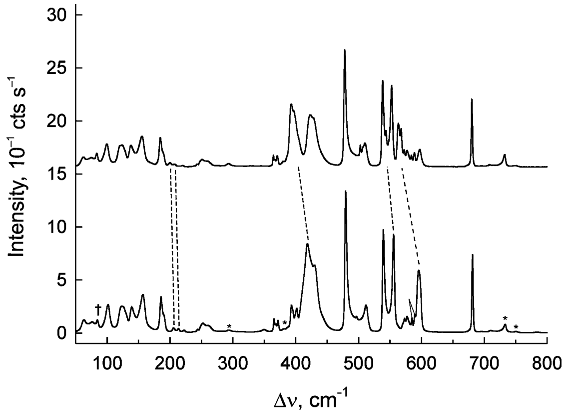

Figure 3. Raman spectra of [Xe_3OF_3][AsF_6] recorded at −160 °C using 1064-nm excitation for natural abundance (lower trace) and 98.6% ^{18}O-enriched (upper trace). Symbols denote FEP sample tube lines (*) and instrumental artifact (†).

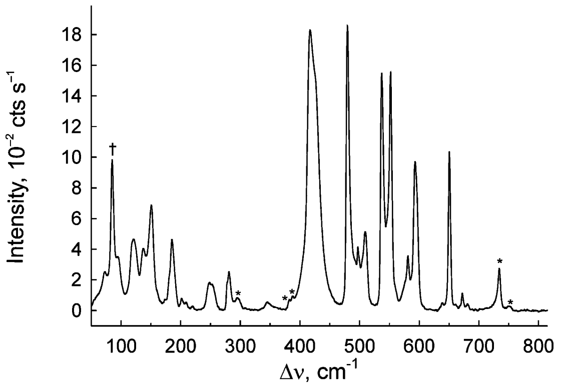

Figure 4. Raman spectra of [Xe_3OF_3][SbF_6] recorded at −160 °C using 1064-nm excitation. Symbols denote FEP sample tube lines (*) and instrumental artifact (†). The spectrum also contains bands attributable to [H_3O][SbF_6] and XeF_2.

the unit cell, but for the most part it is relatively weak and the majority of the observed splittings are the result of site-symmetry lowering.

The frequency assignments for $Xe_3OF_3^+$ are based on calculated frequencies and intensities using DFT methods and are provided in Tables 4 and 5. The frequencies and mode descriptions associated with the $Xe_3OF_3^+$ cation are very similar in both salts; consequently, only the vibrational frequencies of the ^{16}O- and ^{18}O-substituted cations in their AsF_6^- salts are considered in the ensuing discussion.

The majority of the $Xe_3OF_3^+$ vibrational modes are strongly coupled. Although the predicted degree of coupling varies with the level of theory, the predominant components in the mode descriptions remain the same and are therefore used as the basis for the discussion. Moreover, all observed frequency trends and $^{16/18}$O isotopic frequency shifts are in accordance with the calculations. The seven bands observed between 418 and 596 cm^{-1} in the ^{16}O spectrum are assigned to five stretching modes, where two of these bands exhibit a significant low-frequency isotopic shift upon ^{18}O substitution. The highest frequency band at 595.8 cm^{-1} shows a large isotopic shift and splitting (−27.0, −31.4 cm^{-1}; calcd (all methods), −29 to −36 cm^{-1}) and is assigned to the antisymmetric $\nu(Xe_1{-}O_1) - \nu(Xe_2{-}O_1)$ stretching mode. The bands at 418.7, 429.8 cm^{-1} also show very large isotopic shifts [−24.8 and −27.8 cm^{-1}, respectively; calcd (all methods), −16 to −24 cm^{-1}] and are assigned to the symmetric stretching mode, $\nu(Xe_1{-}O_1) + \nu(Xe_2{-}O_1)$, with a small contribution from $\nu(Xe_2{-}F_2) - \nu(Xe_3{-}F_2)$. The bands at 511.9 cm^{-1} and 539.5, 555.7 cm^{-1} are assigned to $\nu(Xe_1{-}F_1)$ and $\nu(Xe_3{-}F_3)$, respectively, with a small contribution from $\nu(Xe_1{-}O_1) - \nu(Xe_2{-}O_1)$ for the latter at the B3LYP and B3PW91 levels of theory (Table 5), and show very small oxygen isotopic dependencies, as expected for essentially pure Xe−F stretching modes. The band at 479.5 cm^{-1} is also insensitive to ^{18}O substitution.

The bands below 260 cm^{-1} are attributed to bending and deformation modes. The weak bands at 206.3, 214.4 cm^{-1} are the only bands that exhibit significant isotopic dependencies [−5.4, −6.3 cm^{-1}; calcd (all methods), −1.6 to 0.0, cm^{-1}] and are assigned to $\delta(F_2Xe_3F_3)_{oop} + \delta(F_1Xe_1O_1)_{oop}$.

(b) [H_3O][AsF_6]·2XeF_2. The Raman and infrared frequencies and intensities for [$H_3{}^{16/18}O$][AsF_6]·2XeF_2 and [D_3O][AsF_6]·2XeF_2, along with their assignments, are provided in Table 6, and the spectrum of [H_3O][AsF_6]·2XeF_2 is shown in Figure 5.

The Raman bands of [H_3O][AsF_6]·2XeF_2 at 190(5), 470(11), and 552(100) cm^{-1} are reminiscent of those observed for free centrosymmetric XeF_2, which occur at 213.2 ($\nu_2(\Pi)$, infrared), 497 ($\nu_1(\Sigma_g{}^+)$, Raman), and 555 ($\nu_3(\Sigma_u{}^+)$, infrared) cm^{-1}.[41] While the Raman activity may be explained by a distortion of XeF_2 with a simultaneous loss of the symmetry center, the high Raman intensity of the 552 cm^{-1} band and the low intensity of the 470 cm^{-1} band suggest that the antisymmetric and the symmetric stretching modes may not be vibrationally strongly coupled. Similar Raman intensity and frequency patterns are also observed for metal coordination complexes of XeF_2 in which XeF_2 is terminally coordinated through one of its fluorine ligands to a metal center such as Cd^{2+}.[43] The high-frequency bands above 800 cm^{-1} (Table 6) are also assigned to the H_3O^+ cation and are comparable to those observed in the [H_3O][AsF_6] salt.[44]

The disordered crystal structure of [H_3O][AsF_6]·2XeF_2 shows four nearest neighbor XeF_2 molecules that are equivalently hydrogen-bonded to each H_3O^+ cation through a fluorine ligand (see X-ray Crystallography). However, the structure is disordered and the high crystal site symmetry of XeF_2 (..2/*m*) does not reveal the lower, precise symmetry of XeF_2 that is apparent from the Raman spectrum, i.e., each H-bonded XeF_2 is asymmetrically bridged to two H_3O^+ cations. For this reason, the XeF_2 modes were assigned under $C_{\infty v}$ symmetry, i.e., $\nu_3(\Pi)$, 190; $\nu_2(\Sigma^+)$, 470; and $\nu_1(\Sigma^+)$, 552 cm^{-1} instead of the $D_{\infty h}$ symmetry suggested by the crystal structure. For similar reasons, and based on the number of observed Raman bands, the AsF_6^- anion modes were assigned under C_{4v} symmetry instead of its higher crystal site symmetry, D_{4h}. Aside from three bands at 190, 470, and 552 cm^{-1} and those above 800 cm^{-1} (vide infra), the remaining bands can be confidently assigned to a distorted AsF_6^- anion under C_{4v} symmetry.

To further establish whether asymmetric coordination of XeF_2 to H_3O^+ accounts for the observed Raman spectrum of [H_3O][AsF_6]·2XeF_2, four $H_3O^+\cdot nXeF_2$ adducts ($n = 1{-}4$) were calculated at the PBE1PBE/aug-cc-pVTZ(-PP) level (Figure 6 and Table S5); the choice of $n = 4$ for the maximum number of XeF_2 molecules coordinated to H_3O^+ was dictated by the local environment of H_3O^+ in the crystal structure of [H_3O][AsF_6]·2XeF_2 (also see Computational Results), which showed that the H_3O^+ cation was coordinated to four neighboring XeF_2 molecules through fluorine (Figure 2).

---

(43) Tavcar, G.; Benkič, P.; Žemva, B. *Inorg. Chem.* **2004**, *43*, 1452–1457.
(44) Christe, K. O.; Schack, C. J.; Wilson, R. D. *Inorg. Chem.* **1975**, *14*, 2224–2230.

Table 5. Calculated[a,b] Vibrational Frequencies and Infrared and Raman Intensities for $Xe_3OF_3^+$

SVWN	BP86	PBE1PBE	B3LYP	B3PW91	MP2	assignment (PBE1PBE)[c]
				$Xe_3{}^{16}OF_3^+$		
604.3(351)[102]	557.5(256)[126]	612.4(55)[159]	580.2(2)[175]	597.8(6)[178]	599.6(127)[131]	$\nu(Xe_3-F_3) + [\nu(Xe_1-O_1) - \nu(Xe_2-O_1)]_{small}$
560.8(181)[222]	522.1(356)[215]	581.4(120)[231]	549.8(139)[213]	566.2(129)[218]	556.4(35)[175]	$\nu(Xe_1-F_1)$
588.0(300)[92]	534.0(322)[20]	626.9(276)[33]	587.1(392)[3]	605.9(365)[8]	656.9(40)[122]	$\nu(Xe_1-O_1) - \nu(Xe_2-O_1)$
441.5(134)[506]	408.8(165)[476]	435.7(172)[509]	419.8(220)[589]	428.4(194)[558]	431.7(299)[955]	$[\nu(Xe_3-F_2) - \nu(Xe_2-F_2)] + [\nu(Xe_1-O_1) + \nu(Xe_2-O_1)]$
420.0(35)[76]	381.3(36)[97]	409.5(21)[350]	390.5(13)[216]	400.7(18)[260]	450.0(63)[43]	$[\nu(Xe_1-O_1) + \nu(Xe_2-O_1)] + [\nu(Xe_2-F_2) - \nu(Xe_3-F_2)]$
219.3(1)[14]	184.3(3)[11]	196.3(<1)[12]	186.9(<1)[11]	187.7(<1)[11]	191.1(<1)[12]	$\delta(F_2Xe_3F_3)_{ip}$
184.3(<0.1)[19]	169.0(<0.1)[19]	195.2(<0.1)[22]	185.6(<0.1)[21]	190.3(<0.1)[21]	195.1(<0.1)[26]	$\delta(F_2Xe_3F_3)_{oop} + \delta(F_1Xe_1O_1)_{oop}$
176.2(2)[1]	162.8(2)[<0.1]	186.3(2)[<]	175.8(2)[2]	181.2(2)[2]	184.3(1)[<1]	$\delta(F_2Xe_3F_3)_{oop} - \delta(F_1Xe_1O_1)_{oop}$
174.1(2)[2]	159.0(3)[<1]	178.8(4)[1]	169.9(4)[1]	174.0(4)[<0.1]	181.0(9)[<1]	$\delta(F_1Xe_1O_1)_{ip}$
128.6(3)[8]	112.1(6)[9]	109.9(4)[14]	105.8(4)[12]	107.7(4)[11]	113.4(4)[14]	$\rho_r(F_1Xe_1O_1)_{ip} + \nu(Xe_2-F_2)$
100.4(3)[<1]	90.2(<1)[<1]	96.9(<1)[<1]	92.2(<1)[<1]	94.7(<1)[<1]	101.1(<1)[<1]	$\rho_t(F_1Xe_1O_1)_{oop} - \rho_t(F_2Xe_3F_3)_{oop}$
99.9(3)[<1]	78.1(6)[2]	92.9(3)[6]	87.8(3)[6]	83.9(2)[7]	95.0(2)[6]	$\delta(Xe_2O_1Xe_1)_{ip} - \rho_r(F_2Xe_3F_3)_{ip}$
40.8(11)[<1]	45.1(2)[<1]	43.1(3)[1]	42.6(4)[1]	43.9(3)[1]	51.1(2)[1]	$\delta(Xe_2O_1Xe_1)_{ip} + \rho_r(F_2Xe_3F_3)_{ip}$
19.6(<1)[<1]	12.3(4)[<1]	5.5(<1)[<0.11]	13.2(1)[<0.1]	19.0(<1)[<0.1]	16.9(2)[<1]	$\rho_t(F_1Xe_1O_1Xe_2)_{oop} - \rho_t(F_2Xe_3F_3)_{oop}$
18.7(<1)[<0.1]	3.2(<1)[<1]	15.0(<1)[<1]	14.6(1)[<1]	11.4(2)[<0.1]	29.4(2)[<0.1]	$\rho_r(F_1Xe_1O_1Xe_2)_{ip} - \rho_r(F_2Xe_3F_3)_{ip}$
				$Xe_3{}^{18}OF_3^+$		
604.3(238)[139]	558.1(209)[139]	615.8(171)[99]	584.1(181)[108]	600.7(173)[107]	609.4(107)[151]	$\nu(Xe_3-F_3) + [\nu(Xe_1-O_1) - \nu(Xe_2-O_1)]_{small}$
566.3(31)[48]	525.9(48)[112]	579.4(180)[281]	547.1(257)[262]	563.4(229)[272]	567.7(59)[197]	$\nu(Xe_1-F_1)$
552.5(505)[218]	503.9(603)[103]	595.2(70)[25]	557.7(61)[9]	575.5(65)[11]	632.5(43)[61]	$\nu(Xe_1-O_1) - \nu(Xe_2-O_1)$
441.3(148)[544]	408.0(188)[522]	434.8(197)[694]	418.4(233)[686]	425.9(210)[686]	435.0(241)[993]	$[\nu(Xe_3-F_2) - \nu(Xe_2-F_2)] + [\nu(Xe_1-O_1) + \nu(Xe_2-O_1)]$
399.6(19)[39]	363.5(20)[52]	391.2(5)[168]	372.9(5)[119]	382.9(6)[135]	419.2(46)[31]	$[\nu(Xe_1-O_1) + \nu(Xe_2-O_1)] + [\nu(Xe_2-F_2) - \nu(Xe_3-F_2)]$
220.0(1)[14]	184.9(3)[11]	193.0(<1)[11]	187.3(<1)[11]	187.7(<1)[11]	202.4(<1)[11]	$\delta(F_2Xe_3F_3)_{ip}$
182.7(<0.1)[17]	167.6(<1)[17]	195.2(<1)[20]	185.3(<1)[19]	189.7(<1)[18]	205.1(<0.1)[21]	$\delta(F_2Xe_3F_3)_{oop} + \delta(F_1Xe_1O_1)_{oop}$
173.5(2)[1]	161.0(2)[1]	183.7(2)[4]	172.9(2)[5]	178.4(2)[4]	190.2(1)[3]	$\delta(F_2Xe_3F_3)_{oop} - \delta(F_1Xe_1O_1)_{oop}$
175.8(2)[3]	159.9(3)[<1]	179.6(4)[<0.1]	171.0(4)[1]	175.2(4)[<1]	185.7(6)[<1]	$\delta(F_1Xe_1O_1)_{ip}$
129.2(3)[9]	112.5(5)[9]	110.1(4)[12]	106.2(4)[12]	108.2(4)[11]	115.5(4)[13]	$\rho_r(F_1Xe_1O_1)_{ip} + \nu(Xe_2-F_2)$
100.8(5)[<1]	89.3(<1)[<1]	96.1(<1)[<1]	91.4(<1)[<1]	94.1(<1)[<1]	105.2(<1)[<1]	$\rho_t(F_1Xe_1O_1)_{oop} - \rho_t(F_2Xe_3F_3)_{oop}$
99.5(<1)[<1]	78.7(6)[2]	87.3(2)[7]	88.3(3)[6]	85.1(2)[7]	96.8(2)[6]	$\delta(Xe_2O_1Xe_1)_{ip} - \rho_r(F_2Xe_3F_3)_{ip}$
41.1(12)[<1]	45.2(2)[<1]	44.8(3)[1]	42.7(4)[1]	43.3(3)[1]	52.2(2)[<1]	$\delta(Xe_2O_1Xe_1)_{ip} + \rho_r(F_2Xe_3F_3)_{ip}$
20.3(<1)[<1]	12.4(5)[<1]	18.7(<1)[<0.1]	13.1(1)[<0.1]	18.7(<1)[<0.1]	31.8(1)[<0.1]	$\rho_t(F_1Xe_1O_1Xe_2)_{oop} - \rho_t(F_2Xe_3F_3)_{oop}$
19.2(<1)[<0.1]	3.1(<1)[<0.1]	11.0(2)[<0.1]	14.6(1)[<1]	10.4(2)[<1]	17.6(2)[<1]	$\rho_r(F_1Xe_1O_1Xe_2)_{ip} - \rho_r(F_2Xe_3F_3)_{ip}$

[a] The aug-cc-pVTZ(-PP) basis set was used. The aug-cc-pVDZ(-PP) values are reported in Table S3. [b] Calculated Raman [infrared] intensities, in units of Å^4 amu^{-1} [km mol^{-1}] appear in parentheses [square brackets]. [c] The atom numbering is as follows: $F_1-Xe_1O-Xe_2{-}{-}{-}F_2-Xe_3-F_3$. Symbols denote stretch (ν), bend (δ), ρ_w (wag), ρ_t (twist), and ρ_r (rock). The abbreviations denote in-plane (ip) and out-of-plane (oop). Only major contributions to the mode descriptions are provided.

Table 6. Observed Vibrational Frequencies[a] for $[H_3O][AsF_6]\cdot2XeF_2$, $[D_3O][AsF_6]\cdot2XeF_2$, and $[H_3{}^{18}O][AsF_6]\cdot2XeF_2$ and Their Assignments

$[H_3O][AsF_6]\cdot2XeF_2$			$[D_3O][AsF_6]\cdot2XeF_2$	$[H_3{}^{18}O][AsF_6]\cdot2XeF_2$	XeF_2	H_3O^+/ D_3O^+	AsF_6^-
Raman,[b,c] 145 °C	Raman,[b] -120°C	IR, -100 °C[d]	Raman,[b] -120 °C	Raman,[b] -120 °C	$C_{\infty v}$	C_{3v}	C_{4v} [O_h]
3292(<1)		3230 br, m	2320(<1)	3110(<1)		$\nu_3(E)$	
3160(<1)							
3077(<1)	3090(<1)		2150(<1)	2860(<1)		$\nu_1(A_1)$	
	2880(<1)						
	1630(<1)	1630, w	1190(<1)	1620(<1)		$\nu_4(E)$	
		830, m				$\nu_2(A_1)$	
710(4)	710(2)	700, vs	711(9)	710(7)			$\nu_8(E)$ [$\nu_3(T_{1u})$]
682(28) 676(12) 670, sh	684(23) 675(10)		683(16) 674(11)	684(21) 678(11)			$\nu_1(A_1)$ [$\nu_1(A_{1g})$] $\nu_6(B_1)$ [$\nu_6(T_{2u})$]
594(8) 587(11)	586(10)	584, w	589(9)	589(9)			$\nu_3(A_1)$ [$\nu_4(T_{1u})$] $\nu_2(A_1)$ [$\nu_2(E_g)$]
552(100) 544, sh	552(100)	552, m	578(86) 550(100)	552(100)	$\nu(Xe–F_{term})$		
470(12)	469(16)	469, s	477(17) 469(19)	470(16)	$\nu(Xe{-}{-}F_{bridge})$		
455(11)	452(16)			455(14)			$\nu_9(E)$ [$\nu_5(T_{2g})$]
370(10) 367(11)	370(11)		369(11)	370(18)			$\nu_4(A_1)$ [$\nu_3(T_{1u})$] $\nu_5(B_1)$ [$\nu_2(E_g)$]
363, sh							$\nu_{10}(E)$ [$\nu_6(T_{2u})$]
241, br	244(1)						$\nu_{11}(E)$ [$\nu_4(T_{1u})$]
216(1)							$\nu_7(B_2)$ [$\nu_5(T_{2g})$]
190(5)	190(1)				$\delta(F_{term}–Xe{-}{-}{-}F_{bridge})$		
142(10)	141(11)		139(8)	140(11)		lattice mode	

[a] Frequencies are in cm^{-1}. [b] Values in parentheses denote relative Raman intensities. [c] Symbols denote shoulder (sh) and broad (br). [d] Symbols denote medium (m), weak (w), very strong (vs), and strong (s).

In $H_3O^+\cdot XeF_2$, the $\nu(XeF_{term})$ and $\nu(XeF_{bridge})$ (Figure 6) modes are coupled, whereas in $H_3O^+\cdot nXeF_2$ ($n = 2-4$), the coupling is mostly interligand, occurring among $\nu(XeF_{term})$-type or $\nu(XeF_{bridge})$-type modes of coordinated XeF_2 molecules. In

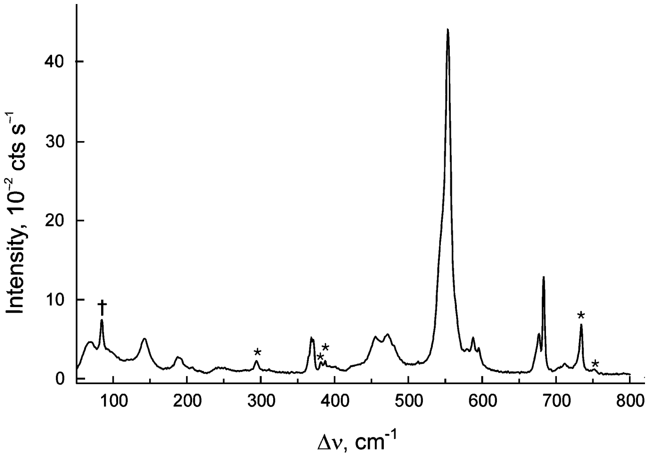

Figure 5. Raman spectrum of $[H_3O][AsF_6]\cdot 2XeF_2$ recorded at −145 °C using 1064-nm excitation. Symbols denote FEP sample tube lines (*) and instrumental artifact (†).

all cases, there is some intramolecular coupling with the associated $\nu(F_{bridge}\text{---}H_{bridge})$ modes. As the number of XeF_2 coordinated molecules increases, the frequencies arising from the $\nu(XeF_{term})$ modes progressively shift to lower frequencies (616, 617 cm^{-1} for $n = 2$; 605, 605, 610 cm^{-1} for $n = 3$; and 581, 599, 604, 608 cm^{-1} for $n = 4$) and those involving $\nu(XeF_{bridge})$ modes shift to higher frequencies (423, 496 cm^{-1} for $n = 2$; 453, 455, 507 cm^{-1} for $n = 3$; 456, 493, 510 cm^{-1} for $n = 4$). Overall, the frequency differences between the $\nu(XeF_{term})$ and $\nu(XeF_{bridge})$ modes decrease as n increases. For $n = 4$, these differences are in good agreement with what is observed experimentally (470 and 552 cm^{-1}). Moreover, the calculated intensities account for the high intensity of the high-frequency band of XeF_2.

The band at 190 cm^{-1} is assigned to a superposition of $F_{term}XeF_{bridge}$-type bending modes and occurs in a region similar to that of free XeF_2 (calcd., 214 cm^{-1}). It is worth noting that this mode is calculated at 214 cm^{-1} for free XeF_2 and between 178 and 245 cm^{-1} for the H_3O^+ adducts. In support of these findings, the infrared spectrum of $[H_3O][AsF_6]\cdot 2XeF_2$ showed bands having the same frequencies as the Raman bands but with reversed relative intensities. The assignments of the 190, 470, and 552 cm^{-1} bands to the XeF_2 moiety of the adduct was further substantiated by the Raman spectra of $[D_3O][AsF_6]\cdot 2XeF_2$ and $[H_3{}^{18}O][AsF_6]\cdot 2XeF_2$, which exhibited only H/D isotopic shifts for the bands above 800 cm^{-1}, confirming their assignments to H_3O^+, whereas the XeF_2 and anion bands were unshifted (Table 6).

A second, more simplistic, model was used in which the frequencies and infrared intensities for XeF_2 were obtained using the B3LYP/aug-cc-pVTZ(-PP) method with the constraint that the two Xe−F bond lengths differed by 0.05, 0.10, and 0.15 Å (Table S6). It was found that with increasing bond length difference, the frequency differences between the two stretching modes also significantly increased and the higher frequency mode became the most intense Raman band, in accordance with our experimental observations. On the basis of the observed frequency difference of 82 cm^{-1} between the experimental 470 and 552 cm^{-1} bands, a Xe−F bond length difference of 0.07 Å was predicted for $[H_3O][AsF_6]\cdot 2XeF_2$; however, this cannot be observed in the present structure due to disorder.

Computational Results. The electronic structures of $Xe_3OF_3^+$ were optimized using DFT methods (SVWN, BP86, PBE1PBE, B3LYP, B3PW1 and MPW1PW91) with the aug-cc-pVDZ(-PP) and aug-cc-pVTZ(-PP) basis sets.[45] Møller−Plesset (MP2) and coupled-cluster (CCSD(T)) methods gave a near-linear bond angle for the Xe−F---Xe moiety, which was also observed for $Xe_2F_3^+$ at the Hartree−Fock level.[27] All optimizations resulted in stationary points with all frequencies real (Tables 3 and 5 and Tables S3 and S4; also see Experimental Section). The $H_3O^+\cdot nXeF_2$ ($n = 1-4$) adducts were optimized at the PBE1PBE/aug-cc-pVTZ(-PP) level of theory. The H_2OF^+ cation was optimized using the CCSD(T) method and its parent neutral species, HOF, has been optimized using the SVWN, PBE1PBE, MP2, and CCSD(T) methods. The calculated vibrational frequencies and infrared intensities show that the infrared bands previously attributed to the H_2OF^+ cation[10] are incompatible with our predictions (Tables S7 and S8). The intermediates, FXeOH and H_2OXeF^+, proposed in eqs 3 and 4, were also optimized using PBE1PBE and CCSD(T) methods (Table S9).

The geometry and vibrational frequencies of XeF_2 were calculated at various levels of theory to serve as a benchmark for $H_3O^+\cdot nXeF_2$ (Table S10). It was concluded that the PBE1PBE/aug-cc-pVTZ(-PP) level gives results that are similar to those of the "expensive" CCSD(T)/aug-cc-pVTZ level of theory, and can thus be used to reliably compute the $H_3O^+\cdot nXeF_2$ systems dealt with in this work.

(a) $Xe_3OF_3^+$. (i) Geometries. The minimum energy structure of $Xe_3OF_3^+$ was found to possess C_s symmetry with all frequencies real (Table 3 and Table S4). Because many of the bond lengths and angles of the $[Xe_3OF_3][PnF_6]$ (Pn = As, Sb) salts in their crystal structures cannot be commented on because of the positional disorder, the calculated structure was relied upon to provide the exact geometry. All methods and basis sets used resulted in similar trends. The two terminal bond lengths (Xe_1-F_1 and Xe_3-F_3) are shorter than the bridge bond lengths (Xe_3-F_2 and $Xe_2\text{---}F_2$), in agreement with those observed for the $Xe_2F_3^+$ cation.[27] The short Xe_2-O_1 bond and long $Xe_2\text{---}F_2$ contact support the $FXeOXe^+\text{---}FXeF$ model proposed for the disordered crystal structures (see X-ray Crystallography). The similar bond lengths calculated for Xe_1-O_1 and Xe_3-F_2 likely account for why it was not possible to split the O/F positions in the crystal structures. The angles about Xe_1, Xe_2, and Xe_3 were found to be slightly less than 180° at all levels of theory, in agreement with the crystal structure and the structure of the $Xe_2F_3^+$ cation.[27] While the range of the Xe_1-O-Xe_2 angles was relatively narrow (116.5 to 121.7°) at all levels of theory, a wider range of values was obtained for the more deformable $Xe_2\text{---}F_2-Xe_3$ angle (142.7−179.9°). Because the structure is disordered, no conclusive statement can be made about which method best reproduces this angle, although DFT (SVWN and BP86) was the only method which gave a significantly bent angle.

Attempts were also made to optimize the $(FXe)_3O^+$ isomer of $FXeOXeFXeF^+$ starting from a planar D_{3h} structure and from a pyramidal C_{3v} structure with an initial Xe−O−Xe angle of 108.5°. In both cases the geometries failed to optimize but the final geometries were very close to planar.

(ii) Gas-Phase XeF^+ Affinities. The XeF^+ affinities of XeF_2, HF, H_2O, and FXeOXeF that yield $HFXeF^+$, H_2OXeF^+, $Xe_2F_3^+$, and $Xe_3OF_3^+$, respectively, were calculated at the PBE1PBE/

---

(45) Basis sets were obtained from the Extensible Computational Chemistry Environment Basis Set Database, version 2/25/04, as developed and distributed by the Molecular Science Computing Facility, Environmental and Molecular Science Laboratory, which is part of the Pacific Northwest Laboratory, P.O. Box 999, Richland, WA 99352.

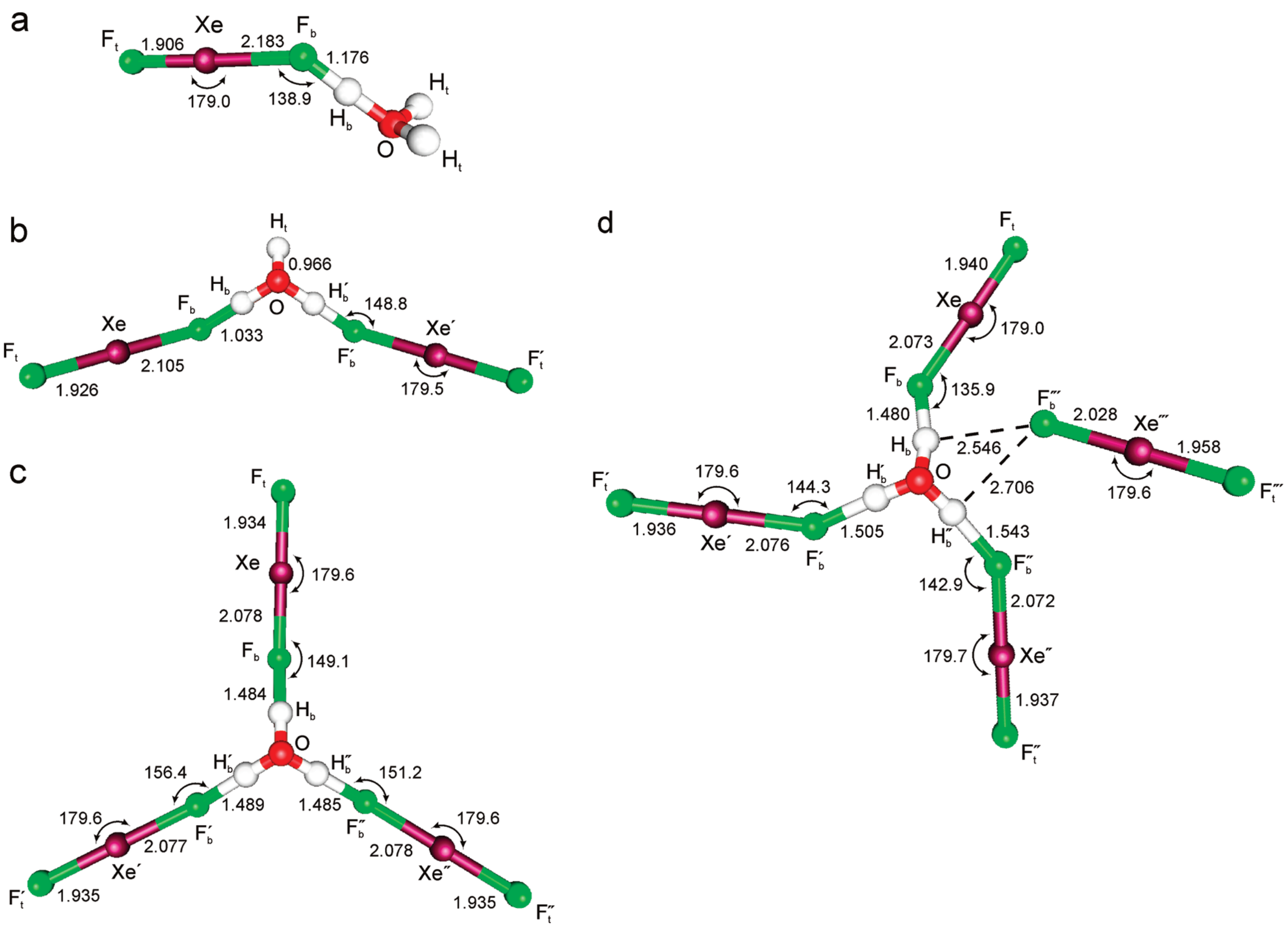

Figure 6. Calculted geometries for $H_3O^+\cdot nXeF_2$ ($n = 1-4$). The atoms labeled F_t, F_t', F_t'', F_t''' and F_b, F_b', F_b'', F_b''' are referred to in the discussion as F_{term} and F_{bridge}, respectively.

Table 7. Calculated[a] Natural Charges, Valencies, and Bond Orders for $FXeOXeFXeF^+$

	SVWN	BP86	PBE1PBE	B3LYP	B3PW91	MPW1PW91
			natural charges [valencies]			
F_1	−0.511 [0.362]	−0.491 [0.341]	−0.528 [0.358]	−0.520 [0.343]	−0.520 [0.353]	−0.527 [0.356]
Xe_1	1.153 [0.707]	1.125 [0.656]	1.210 [0.659]	1.195 [0.639]	1.195 [0.654]	1.211 [0.655]
O_1	−0.855 [0.909]	−0.802 [0.860]	−0.887 [0.881]	−0.859 [0.863]	−0.868 [0.874]	−0.884 [0.876]
Xe_2	1.095 [0.647]	1.063 [0.600]	1.129 [0.617]	1.109 [0.601]	1.116 [0.611]	1.126 [0.613]
F_2	−0.624 [0.341]	−0.625 [0.303]	−0.686 [0.293]	−0.679 [0.280]	−0.679 [0.292]	−0.687 [0.292]
Xe_3	1.218 [0.599]	1.197 [0.564]	1.269 [0.565]	1.258 [0.543]	1.257 [0.561]	1.270 [0.562]
F_3	−0.477 [0.394]	−0.466 [0.371]	−0.508 [0.376]	−0.503 [0.362]	−0.501 [0.373]	−0.508 [0.374]
			bond order			
Xe_1-F_1	0.352	0.331	0.345	0.332	0.341	0.343
Xe_1-O_1	0.358	0.330	0.321	0.316	0.321	0.319
O_1-Xe_2	0.537	0.516	0.545	0.534	0.539	0.542
Xe_2-F_2	0.109	0.085	0.077	0.073	0.078	0.076
F_2-Xe_3	0.214	0.202	0.199	0.191	0.198	0.198
Xe_3-F_3	0.383	0.360	0.363	0.349	0.360	0.361

[a] aug-cc-pVTZ(-PP).

aug-cc-pVTZ(-PP) level of theory (Table S11). The standard heats and Gibbs free energies (kJ mol^{-1}) for the reactions of XeF^+ with HF ($\Delta H°$, −48.35; $\Delta G°$, −81.45), H_2O ($\Delta H°$, −118.75; $\Delta G°$, −156.46), XeF_2 ($\Delta H°$, −122.83; $\Delta G°$, −155.97), and FXeOXeF ($\Delta H°$, −206.74; $\Delta G°$, −238.40) are all exothermic and spontaneous, with $O(XeF)_2$ exhibiting the greatest affinity for XeF^+. Xenon difluoride and water have comparable values, which are intermediate in the series, with HF exhibiting the lowest affinity.

(iii) Natural Bond Orbital (NBO) Analysis. The NBO analyses (Table 7) were carried out for all DFT-optimized gas-phase geometries and provide further support for the $FXeOXe^+$---FXeF model. Similar trends in calculated valencies, bond orders, and charges were found at all levels, but only the PBE1PBE values are considered in the ensuing discussion.

All of the calculated bond orders are significantly less than 1 and are consistent with the highly polar natures of these bonds. There is a strong covalent interaction between Xe_2 and O_1

(0.545) and a very weak bonding interaction between Xe_2 and F_2 (0.077), which supports the choice of $FXeOXe^+$---FXeF as the dominant resonance structure (see X-ray Crystallography). Moreover, the group charges, $FXeOXe^+$ (0.924), FXeF (0.075) and $FXeO^-$ (−0.205), $^{2+}$XeFXeF (1.204), also support the former bonding description.

(b) $H_3O^+ \cdot nXeF_2$ (n = 1−4). To support the vibrational assignments for $[H_3O][AsF_6] \cdot 2XeF_2$, four $H_3O^+ \cdot nXeF_2$ adducts (n = 1−4) were calculated at the PBE1PBE/aug-cc-pVTZ(-PP) level (Figure 6 and Table S5). The $H_3O^+ \cdot XeF_2$ and $H_3O^+ \cdot 2XeF_2$ adducts both optimized under C_s symmetry, whereas $H_3O^+ \cdot 3XeF_2$ and $H_3O^+ \cdot 4XeF_2$ both optimized under C_1 symmetry. Coordination of XeF_2 to H_3O^+ gives rise to a slight asymmetry in the Xe−F bond lengths, the longer bond being that in which its fluorine atom hydrogen bonds to the H_3O^+ cation. The $Xe{-}F_{term}$ bond lengths increase as the number of coordinated XeF_2 molecules increases, while the $Xe{-}F_{bridge}$ bond lengths decrease. Therefore, the asymmetry, which is measured by the bond length difference, $d(Xe{-}F_{bridge}) - d(Xe{-}F_{term})$, decreases as n increases. Correspondingly, the difference in average frequencies, $\nu(XeF_{term})_{av} - \nu(XeF_{bridge})_{av}$, also decreases with increasing n. The F_{bridge}---H_{bridge} distances range from 1.033 Å (n = 2) to 1.543 Å (n = 4) and indicate that the contacts between the XeF_2 molecules and the H_3O^+ cation are significant. A second approach, which fixed the Xe−F distances of XeF_2 by contracting one Xe−F bond and elongating the other by the same amount, resulted in calculated frequencies that showed a similar trend (Table S6).

(c) H_2OF^+. A series of high-level theoretical calculations using DFT and ab initio (MP2 and CCSD(T)) methods (Table S7) were run for both HOF and DOF to serve as benchmarks. The best agreement between observed and calculated geometries was obtained at the CCSD(T)/aug-cc-pVTZ level. This level also proved to be good for reproducing various trends among frequencies as well as isotopic shifts and was consequently used for the study of the H_2OF^+ cation. It is worth noting that the intensity trends were reproduced at all levels.

(i) Vibrational Spectra of H_2OF^+. The geometries and vibrational frequencies of $H_2{}^{16}OF^+$, $D_2{}^{16}OF^+$, $H_2{}^{18}OF^+$, and $D_2{}^{18}OF^+$ were calculated at the CCSD(T)/aug-cc-pVTZ level (Table S8) and do not match the reported spectra in several key respects: (1) most of the intensities do not fit; for example, $\nu_3(A')$ is predicted to be a strong band but is either observed only as a weak band or is not observed; $\nu_4(A')$ is predicted to be weak but was reported as strong, and $\nu_6(A'')$ is calculated to have zero intensity and was reported to be of medium intensity; (2) the observed and calculated isotopic shifts are very different for $\nu_2(A')$, $\nu_4(A')$, and ν_5(A”) of $D_2{}^{16}OF^+$ and $\nu_2(A')$ and $\nu_4(A')$ of $D_2{}^{18}OF^+$; and (3) in the previously reported infrared spectra, $\nu_5(A'')$, which was assigned as $\nu_{as}(OX_2)$ (X = H, D), was shown to be a very intense band, yet it is not observed in the experimental vibrational spectra of the alleged $H_2{}^{18}OF^+$ and $D_2{}^{18}OF^+$ cations. In summary, there can be no doubt that the previously reported spectra cannot arise from the H_2OF^+ cation. The absence of the strong infrared bands around 470 and 552 cm^{-1} for the XeF_2 moieties of $[H_3O][AsF_6] \cdot 2XeF_2$ also rules out the presence of this adduct in the previously reported spectra.[10]

(ii) ^1H and ^{19}F NMR Chemical Shifts for H_2OF^+. Chemical shifts were also calculated for H_2OF^+, HOF, $H_2NF_2^+$, and HNF_2 by the GIAO method using CCSD(T)/aug-cc-pVDZ optimized geometries. The results are summarized in Table 1 and are compared with the reported values for H_2OF^+,[10] HOF,[9] $H_2NF_2^+$,[31] and HNF_2.[30] Again, it can be seen that the ^{19}F value previously attributed[10] to H_2OF^+ is in marked disagreement with calculated values. The reported value differs by almost 440 ppm from the predicted value and is unlikely to arise from H_2OF^+. In contrast, agreement between calculated and observed values for HOF, $H_2NF_2^+$, and HNF_2 is ca. ±6 ppm. This again supports the experimental evidence presented above that the previously published report of the H_2OF^+ cation is erroneous. The broad ^{19}F NMR signals at −57.8 and −68.0 ppm were attributed to AsF_6^- and H_2OF^+, respectively.[10] The latter resonance actually arises from AsF_6^-, which occurs at −68.5 ppm (this work).

(d) FXeOH and H_2OXeF^+. The geometries and harmonic frequencies for $FXe^{16}OH$, $FXe^{18}OH$, $FXe^{16}OD$, $H_2{}^{16}OXeF^+$, $H_2{}^{18}OXeF^+$, and $D_2{}^{16}OXeF^+$ were calculated using the PBE1PBE and CCSD(T) (values in square brackets) methods and the aug-cc-PVTZ(-PP) basis set, resulting in optimized C_s geometries having all frequencies real (Table S9). The calculations show that FXeOH and H_2OXeF^+ are indeed viable species and could therefore be possible intermediates in Scheme 1.

The calculated geometry of the H_2OXeF^+ cation suggests that XeF^+ forms an oxygen-bonded, donor−acceptor adduct with water, having an Xe---O bond length of 2.320 [2.344] Å, an Xe−F bond length of 1.899 [1.905] Å, and an F−Xe−O angle close to 180° (178.4 [178.3]°). The Xe−F bond length is significantly shorter than that of XeF_2 (1.986 [1.991] Å, Table S10; 2.00(1) Å[41] but longer than that of XeF^+ (1.84(1) Å in $[XeF][Sb_2F_{11}]$[46]). The near-linear F−Xe−O angle (177.9 [177.8]°) of FXeOH is also near linear with Xe−O (2.038 [2.062] Å) and Xe−F (2.029 [2.036] Å) bond lengths that are shorter and longer, respectively, than in H_2OXeF^+.

Conclusion

The reactions of $[XeF][PnF_6]$ (Pn = As, Sb) with H_2O in HF solution depend strongly on the conditions and result in the formation of two new xenon species, $[Xe_3OF_3][PnF_6]$ (Pn = As, Sb) and $[H_3O][AsF_6] \cdot 2XeF_2$. The $Xe_3OF_3^+$ cation represents the first example of a Xe(II) oxide fluoride, and its formation is strong evidence for the formation of FXeOH as an unstable intermediate in the hydrolysis of XeF_2. The $[Xe_3OF_3][PnF_6]$ salts have been characterized by Raman spectroscopy and single-crystal X-ray diffraction, establishing the presence of the Z-shaped $Xe_3OF_3^+$ cation. The $[H_3O][AsF_6] \cdot 2XeF_2$ adduct and its D- and ^{18}O- isotopically enriched counterparts have also been characterized by Raman and infrared spectroscopies and single-crystal X-ray diffraction. The geometries and vibrational assignments for the $Xe_3{}^{16/18}OF_3^+$ cation and the $[H/D_3{}^{16/18}O][AsF_6] \cdot 2XeF_2$ adduct are supported by quantum-chemical calculations.

The present study failed to provide evidence for the presence of the previously claimed H_2OF^+ cation in solutions of XeF^+ and H_2O in HF, the oxygenation of ClF_3 by these solutions, and the protonation of HOF in HF/AsF_5 or $HOSO_2F/SbF_5$. The plausibility of the ^{19}F chemical shift, previously attributed to H_2OF^+, is also rendered highly questionable by the results of quantum-chemical calculations, which show very poor agreement between the predicted and the previously reported values.

Experimental Section

Apparatus and Materials. All manipulations involving air-sensitive materials were carried out under strictly anhydrous

---

(46) Bartlett, N. *Endeavour* **1972**, *31*, 107–112.

conditions as previously described.[47] Volatile materials were handled on vacuum lines constructed of nickel, stainless steel, and FEP. Nonvolatile materials were handled in the atmosphere of a drybox or a glovebag. Reaction vessels/Raman sample tubes and NMR sample tubes were fabricated from 0.25-in. o.d. and 4-mm o.d. FEP tubing, respectively, and outfitted with Kel-F or 316 stainless steel valves. All reaction vessels and sample tubes were rigorously dried under dynamic vacuum prior to passivation with ClF_3 or 1 atm of F_2 gas.

Commercially available D_2O (99.9% D, MSD Isotopes), enriched H_2O (^{16}O, 35.4%; ^{17}O, 21.9%; ^{18}O, 42.7%; Office de Rayonnements Ionisants, Saclay, France), $H_2{}^{18}O$ (Isotec, 98.6% ^{18}O), DF, AsF_5 and BiF_5 (Ozark-Mahoning) were used as received. Antimony pentafluoride, SbF_5, (Ozark-Mahoning Co.) and ClF_3 (Matheson) were purified by fractional condensation prior to use. Literature methods were used for the purification and/or syntheses of XeF_2,[23] XeF_4,[48] $[XeF][AsF_6]$,[49] $[H_3O][AsF_6]$,[44] $[H_3O][SbF_6]$,[44] AsF_5,[23] BrF_5 (Matheson and Ozark-Mahoning),[50] and HF (Harshaw Chemicals).[50]

Synthesis and Attempted Protonation of HOF. The preparation of HOF was carried out using a modification of the procedure published by Appelman and Jache.[29] A recirculating loop was built, consisting of three 0.5-in. o.d. FEP U-traps and a stainless-steel bellows pump (Model MB-21, Metal Bellows Corp.). The first U-trap (the reactor) was maintained at −45 °C and was filled with Teflon Raschig rings, wetted with 2 mL of distilled water. The second U-trap was maintained at −78 °C to trap unreacted H_2O and HF, while the third U-trap was maintained at −196 °C to trap the desired HOF and any OF_2 byproduct. The −196 °C trap could be closed by Teflon valves and was connected to a pressure gauge, which was protected by a Teflon diaphragm, a Teflon infrared cell with BaF_2 windows, and a third connector for withdrawing HOF samples. Any OF_2 byproduct could be taken off either as a fore run at low temperatures or by pumping at −142 °C. In place of neat F_2, a 4:1 mixture of N_2:F_2 at a pressure of about 400 Torr was used. The whole recirculating loop was connected to a stainless-steel Teflon vacuum line to allow evacuation and the introduction of other reagents.

A mixture of 1 mmol of pure HOF and 0.4 mL of liquid SO_2ClF was prepared in the HOF U-trap and condensed into a 4-mm FEP NMR tube at −196 °C, followed by heat sealing of the FEP tube. In a second experiment, a 3-fold excess of a 1:1 mixture of HF and AsF_5 was added to the NMR sample, which was maintained and recorded at −78 °C. In a third experiment, an excess of a 1:1 mixture of $HOSO_2F$ and SbF_5 was first introduced into the NMR tube, and the HOF/SO_2ClF mixture was condensed onto it at −196 °C.

Reactions of $[XeF][PnF_6]$ (Pn = As, Sb) and H_2O in HF Solution. In a typical experiment, H_2O (18.0 μL, 1.00 mmol) was syringed into a 0.75-in. o.d. FEP reactor. The ampoule was closed with a stainless-steel valve, cooled to −196 °C, and evacuated. Approximately 5 mL of anhydrous HF was condensed into the reactor at −196 °C, and the mixture was homogenized at room temperature. The reactor was transferred to a drybox and cooled to −196 °C, and $[XeF][AsF_6]$ (0.339 g, 1.00 mmol) was added. The cold reactor was evacuated on the vacuum line, allowed to warm to −64 °C, kept at this temperature for 12 h, and checked for xenon evolution by monitoring the pressure above the liquid phase with a pressure gauge. No gas evolution was observed, and a clear colorless solution of $[H_3O][AsF_6]$ and XeF_2 resulted. The HF solvent was pumped off at −64 °C, leaving behind a white solid residue (0.360 g; the weight calculated for 1.00 mmol of a 1:1 molar mixture of $[H_3O][AsF_6]$ and XeF_2 was 0.377 g). The product was characterized by low-temperature infrared and Raman spectroscopy.

Experiments involving $[XeF][SbF_6]$ were carried out in an fashion analogous to those involving $[XeF][AsF_6]$. In one case, the low-temperature Raman spectrum of a sample of $[H_3O][SbF_6]$ and XeF_2, obtained from an HF solution of $[XeF][SbF_6]$ and H_2O at −64 °C, was recorded with a relatively high laser power of 1.6 W and revealed some additional features. In addition to the main products, $[H_3O][SbF_6]$ and XeF_2, the Raman spectrum showed a small amount of a new compound with a relatively strong band at 452 cm^{-1}. Furthermore, careful temperature cycling in the laser beam between −130 and −50 °C resulted in complete conversion of the XeF_2 to $[XeF][SbF_6]$ and $[Xe_2F_3][SbF_6]$, probably arising from local heating effects. After warming briefly to room temperature, the final products were $[XeF][SbF_6]$, $[Xe_2F_3][SbF_6]$, and $[H_3O][SbF_6]$.

Synthesis of $[Xe_3OF_3][AsF_6]$. (a) Reaction of $[XeF][AsF_6]$ and H_2O in HF. In a typical experiment, 8.0 μL of H_2O (0.44 mmol) was syringed into a 0.25-in. o.d. FEP reaction tube equipped with a Kel-F valve inside a well-purged dry nitrogen-filled glovebag. Approximately 0.4 mL of HF was condensed into the tube at −196 °C, and the water was mixed with the HF at room temperature. After the FEP tube was transferred into a drybox at room temperature, 0.1549 g (0.4566 mmol) of $[XeF][AsF_6]$ was added to the frozen H_2O/HF mixture followed by warming to −78 °C outside the drybox. The sample was maintained at −78 °C.

The reaction rate was found to be strongly dependent on the concentration, reaction temperature, and the degree of initial mixing. Without initial agitation, small amounts of $[XeF][AsF_6]$ were detected in the Raman spectrum of the precipitate at −78 °C after ca. 1 week. After thorough mixing at an initial concentration of 1.77 M H_2O, $[H_3O][AsF_6]\cdot 2XeF_2$ and $[Xe_2F_3][AsF_6]$ were formed after only 2 h with $[XeF][AsF_6]$ being completely reacted at −78 °C, and a significant amount of $[Xe_3OF_3][AsF_6]$ was present after 12 h. At H_2O concentrations of 0.26 M, $[H_3O][AsF_6]\cdot 2XeF_2$ was formed within approximately 1 day, while $[Xe_2F_3][AsF_6]$ was the major species in the solid precipitate after approximately 2 days at −78 °C. Upon standing for a further 5 days at −78 °C, $[Xe_3OF_3][AsF_6]$ became the major species.

An NMR sample was prepared by loading, inside the drybox, 0.20849 g (0.6146 mmol) of $[XeF][AsF_6]$ into a 10-mm o.d. FEP tube fused to a piece of 0.25-in. o.d. FEP tubing connected to a Kel-F valve. Approximately 2.35 mL of HF was condensed onto the $[XeF][AsF_6]$ at −196 °C. The $[XeF][AsF_6]$ was dissolved upon warming the mixture to room temperature. Inside the drybox, 11.5 μL (0.60 mmol) of $H_2{}^{17}O$ was syringed onto the frozen $[XeF][AsF_6]$/HF mixture and transferred outside the drybox where the sample was heat sealed and stored at −196 °C until characterized by NMR spectroscopy.

(b) Reaction of $[H_3O][PnF_6]$ (Pn = As, Sb) with XeF_2. (i) In HF Solution. The syntheses of high-purity $[Xe_3OF_3][PnF_6]$ involved dissolution at −50 °C of near-equimolar amounts of $[H_3O][PnF_6]$ and XeF_2 (up to ca. 20 mol % excess XeF_2) at ca. 0.2−3 M H_3O^+ in a 0.25-in. FEP reactor which had a side arm fused to it. The solution was rapidly warmed to −35 °C for ca. 30 s and immediately cooled to −50 °C. After 5 min at −50 °C, a voluminous deep red-orange precipitate of $[Xe_3OF_3][PnF_6]$ formed. The reaction mixture was maintained at −50 °C for an additional 20−30 min to ensure the reaction was complete. Unreacted XeF_2 and/or $[H_3O][PnF_6]$, as well as $[Xe_2F_3][PnF_6]$ byproduct, were soluble and were decanted from the settled precipitate at −50 °C into the side arm of the reactor at −78 °C. The product, $[Xe_3OF_3][PnF_6]$, decomposed under HF above −30 °C with Xe gas evolution.

The critical effect of initial reaction temperature on $Xe_3OF_3^+$ cation formation was demonstrated by a related synthesis at a lower temperature (−64 °C). A solution of freshly prepared $[H_3O][AsF_6]$ (1.00 mmol; ca. 0.2 M) in anhydrous HF (ca. 5 mL) was cooled to −196 °C and XeF_2 (1.00 mmol; ca. 0.2 M) was added in the drybox., the mixture was warmed to −64 °C for 12 h. The resulting

---

(47) Casteel, W. J., Jr.; Kolb, P.; LeBlond, N.; Mercier, H. P. A.; Schrobilgen, G. J. *Inorg. Chem.* **1996**, *35*, 929–942.

(48) Chernick, C. L.; Malm, J. G. *Inorg. Synth.* **1966**, *8*, 254–258.

(49) Gillespie, R. J.; Landa, B. *Inorg. Chem.* **1973**, *12*, 1383–1389.

(50) Emara, A. A. A.; Schrobilgen, G. J. *Inorg. Chem.* **1992**, *31*, 1323–1332.

clear, colorless solution did not show any signs of xenon evolution during this time period, nor did $[Xe_3OF_3][AsF_6]$ crystallize from solution. The solvent was pumped off at −64 °C, leaving behind a solid white residue, which was identified by low-temperature Raman spectroscopy as a mixture of $[H_3O][AsF_6]\cdot 2XeF_2$, $[XeF][AsF_6]$, and $[Xe_2F_3][AsF_6]$.

(ii) As a Solid Mixture. A 1:1 molar solid mixture of $[H_3O][AsF_6]$ (0.1626 g, 0.782 mmol) and XeF_2 (0.1324 g, 0.782 mmol) were slowly warmed in a dynamic vacuum to room temperature. The volatile products were trapped at −196 °C and identified by infrared spectroscopy as HF and AsF_5. During the warm-up, the color of the sample changed from white to red-orange and back to white. The white solid residue (0.186 g; weight calculated for 0.2065 mmol of $[Xe_2F_3][AsF_6]$ and 0.413 mmol of $[H_3O][AsF_6]$, 0.190 g) was identified by Raman spectroscopy as a mixture of $[Xe_2F_3][AsF_6]$ and $[H_3O][AsF_6]$.

Reaction of $[XeF][AsF_6]/H_2O$ with ClF_3. An equimolar solution of $[XeF][AsF_6]$ and H_2O in HF solvent was reacted for 12 h at −64 °C, and an equimolar amount of ClF_3 was added at −196 °C. The mixture was warmed to −78 °C. After about 2 min, a red suspension formed that eventually turned white. The mixture was allowed to slowly warm to room temperature, and the volatile products were pumped off at room temperature, leaving behind a white solid residue that was shown by infrared spectroscopy to contain $[ClO_2][AsF_6]$ but no $[ClOF_2][AsF_6]$.

Reaction of XeF_2 and $[H_3O][AsF_6]$ in BrF_5 Solution. Inside the drybox, 0.0419 g (0.2015 mmol) of $[H_3O][AsF_6]$ and 0.0372 g (0.2197 mmol) of XeF_2 were loaded at low temperature (ca. −150 °C) into a 4-mm o.d. FEP tube connected to a Kel-F valve. Approximately 0.25 mL of BrF_5 was condensed into the tube at −196 °C, and the FEP tube was heat-sealed under dynamic vacuum.

Reaction of XeF_4 and $[H_3O][SbF_6]$ in HF Solution. An NMR sample was prepared using a 4-mm o.d. FEP tube equipped with a Kel-F valve. Inside the drybox, 0.09110 g (0.3576 mmol) of $[H_3O][SbF_6]$ and 0.07908 g (0.3815 mmol) of XeF_4 were loaded into the FEP tube at low temperature (ca. −140 °C), followed by condensation of ca. 0.2 mL HF onto the solid mixture. After sealing, the sample was warmed to 0 °C, resulting in apparent incomplete dissolution of the solid white reaction mixture and gas evolution. The Raman spectrum of the solid under frozen HF showed bands assigned to the reduction products, $[XeF][SbF_6]$ and $[Xe_2F_3][SbF_6]$.

Crystal Growth. Single crystals suitable for X-ray structure determinations were grown from HF solvent inside a dry stream of cooled nitrogen gas as previously described. With the exception of $[Xe_3OF_3][SbF_6]$, the 0.25-in. o.d. vessels used for crystal growth were equipped with side arms to permit decantation of the supernatant once crystal growth was completed.

(a) $[Xe_3OF_3][AsF_6]$. Inside a well-purged glovebag, 11.0 μL (0.61 mmol) of H_2O was syringed into a 0.25-in. o.d. FEP tube equipped with a Kel-F valve that had a 0.25-in. o.d. FEP side arm fused to it. Approximately 0.5 mL of HF was condensed into the tube at −196 °C, and the contents were mixed at room temperature. After transferring the reaction tube into a drybox at room temperature, 0.2082 g (0.6138 mmol) of $[XeF][AsF_6]$ was added to the frozen H_2O/HF mixture followed by warming to −78 °C outside the drybox. After maintaining the sample at −78 °C for ca. 3 weeks, red-orange dendrimeric clusters of crystals appeared above an orange-brown precipitate. The crystals were isolated by decanting the supernatant into the side arm of the reactor, which was cooled to −196 °C and subsequently heat-sealed off, followed by removal of the residual HF solvent from the crystals under dynamic vacuum at −78 °C. The crystal used in the X-ray structure determination had the dimensions 0.14 × 0.12 × 0.10 mm^3.

(b) $[Xe_3OF_3][SbF_6]$; Reaction of XeF_4 with $[H_3O][SbF_6]$. Inside the drybox, 0.07226 g (0.2836 mmol) of $[H_3O][SbF_6]$ was transferred to a 0.25-in. o.d. FEP tube fitted with a Whitey ORM2 stainless steel valve. Approximately 0.5 mL of HF was condensed into the tube at −78 °C. Inside the drybox, 0.0671 g (0.3122 mmol) of XeF_4 was added to the frozen $[H_3O][SbF_6]$/HF mixture (ca. −140 °C) followed by brief warming to 0 °C outside the drybox to solubilize XeF_4 in the HF solvent. The sample was cooled to −78 °C and maintained at that temperature for several months. Inspection of the sample revealed deep red-orange, needle-shaped crystals above a white crystalline precipitate in a colorless supernatant. The white material was shown to be $[Xe_2F_3][SbF_6]$ by recording the Raman spectrum under frozen HF. Crystals were isolated by decanting the supernatant into the side arm of the reactor as described above. The crystal used for the X-ray structure determination had the dimensions 0.10 × 0.10 × 0.06 mm^3.

(c) $[H_3O][AsF_6]\cdot 2XeF_2$. Inside the drybox, 8.0 μL (0.44 mmol) of H_2O was syringed into a 0.25-in o.d. FEP T-shaped reactor fitted with a Kel-F valve. The reactor was then removed to a metal vacuum manifold where ca. 0.5 mL of anhydrous HF was distilled onto the sample. The reactor and contents were allowed to warm to ambient temperature and mixed. The reactor, back pressured to ca. 1 atm with dry N_2 gas at −78 °C, was then transferred to the drybox where 0.16178 g (0.47695 mmol) of $[XeF][AsF_6]$ was transferred into the reactor that was frozen at ca. −140 °C. The sample was then immediately removed from the drybox, allowed to warm to −68 °C, and mixed for a period of 12 min, resulting in the formation of a colorless precipitate. The vessel was briefly warmed above −68 °C and mixed before being inserted into the cold flow (ca. −70 °C) of the crystal growing apparatus. Crystals were grown slowly with the temperature being decreased at a rate of 0.5 °C min^{-1} to ca. −85 °C, after which the HF solvent was decanted into the side arm of the reactor, which was heat-sealed off under vacuum and removed. The residual HF solvent was then removed under vacuum at ca. −85 °C. The crystal used for the X-ray structure determination had the dimensions 0.14 × 0.14 × 0.14 mm^3.

X-ray Structure Determinations of $[Xe_3OF_3][PnF_6]$ (Pn = As, Sb) and $[H_3O][AsF_6]\cdot 2XeF_2$. Crystals of $[Xe_3OF_3][PnF_6]$ (Pn = As, Sb) and $[H_3O][AsF_6]\cdot 2XeF_2$ were mounted under a flow of cold nitrogen as previously described,[51] and data were collected at −173, −110, and −145 °C, respectively.

(a) Collection and Reduction of X-ray Data. Data were collected using a P4 Siemens diffractometer, equipped with a Siemens SMART 1K charge-coupled device (CCD) area detector (using the program SMART)[52] and a rotating anode using graphite-monochromated Mo Kα radiation (λ = 0.71073 Å). The crystal-to-detector distances were 5.0120, 4.9840, and 4.9870 cm for $2XeF_2\cdot[H_3O][AsF_6]$, $[Xe_3OF_3][AsF_6]$, and $[Xe_3OF_3][SbF_6]$, respectively, and the data collection was carried out in a 512 × 512 pixel mode using 2 × 2 pixel binning. Complete spheres of data were collected to better than 0.8 Å resolution. Processing was carried out by using the program SAINT,[53] which applied Lorentz and polarization corrections to three-dimensionally integrated diffraction spots. The program SADABS[54] was used for the scaling of diffraction data, the application of a decay correction, and an empirical absorption correction based on redundant reflections.

(b) Solution and Refinement of the Structures. The structure determinations were performed as previously described using the program SHELXTL.[55] The program XPREP[55] was used to confirm the unit cell dimensions and the crystal lattices. Solutions were obtained using direct methods that located the Xe and As or Sb atoms in the structures of $[H_3O][AsF_6]\cdot 2XeF_2$, $[Xe_3OF_3][AsF_6]$, and $[Xe_3OF_3][SbF_6]$. The positions of all fluorine and oxygen atoms were revealed in successive difference Fourier syntheses. The

---

(51) Gerken, M.; Dixon, D. A.; Schrobilgen, G. J. *Inorg. Chem.* **2000**, *39*, 4244–4255.

(52) *SMART, release 5.054*; Siemens Energy and Automation Inc.: Madison, WI, 1999.

(53) *SAINT+, release 6.01*; Siemens Energy and Automation Inc.: Madison, WI, 1999.

(54) Sheldrick, G. M. *SADABS (Siemens Area Detector Absorption Corrections), version 2.10*; Siemens Analytical X-ray Instruments, Inc.: Madison, WI, 2004.

(55) Sheldrick, G. M. *SHELXTL, release 5.1*; Siemens Analytical X-ray Instruments, Inc.: Madison, WI, 1998.

PLATON program[56] was used to check for possible alternative space groups. Despite the presence of multiple disorders in each structure, the final refinements are quite acceptable.

(i) [Xe_3OF_3][PnF_6]. The original cells were confirmed, and the lattice exceptions were unambiguous, showing the lattice to be monoclinic primitive. An examination of the E-statistics gave a value that was intermediate between the expected values for a centrosymmetric and a noncentrosymmetric space group; however, this parameter was considered with caution because of the large number of heavy atoms in the structure. The presence of a *c*-glide was evident from the systematic absences, but the 0*k*0 reflections (k = odd) were either weak or absent; hence a first choice for the space group was $P2_1/c$. Although a reasonable solution could be obtained in this space group for both salts, comparison of the Raman spectra of the AsF_6^- and SbF_6^- salts and the results of a factor-group analysis using $P2_1/c$ revealed an inconsistency in the case of the AsF_6^- salt. To see all the modes observed experimentally, the site symmetry could not be C_i as implied by $P2_1/c$ because the bands originating from the ungerade modes (T_{1u} and T_{2u}) were observed. At this point, the tolerance (i.e., minimum $I/\sigma(I)$ GAP) was changed before the space group was selected; this gave rise to new options for the choice of space group. The structure of the AsF_6^- salt was resolved using the space group *Pc*, and the factor-group analysis was redone accordingly, and accounted for the factor-group components associated with the T_{1u} and T_{2u} bands (Tables S1 and S2; also see Raman Spectroscopy).

In the structure of [Xe_3OF_3][SbF_6], the Xe(2) atom was located on a general position which resulted in a positional disorder, i.e., Xe(2) gives rise to Xe(2A) by symmetry. In the structure of [Xe_3OF_3][AsF_6], Xe(2) and Xe(2A) are not related by symmetry. Electroneutrality required the presence of an oxygen bridge in the $Xe_3OF_3^+$ cation which, in conjunction with the split Xe(2) position, results in two possible disorder models (see Results and Discussion). The PnF_6^- anions are disordered between two orientations. The final refinements were obtained by using data that had been corrected for absorption and by introducing anisotropic thermal parameters for all the atoms. During the final stages of the refinement, all reflections with $F^2 < -2\sigma(F^2)$ were suppressed, extinction parameters were used, and weighting factors recommended by the refinement program were introduced.

(ii) [H_3O][AsF_6]·2XeF_2. The atom at the special position (*m.mm*) was defined as the oxygen of the H_3O^+ cation, and as a consequence, the disordered positions of hydrogen atoms about the oxygen atom could not be found in the difference map. The possible interpretations of the crystal structure of [H_3O][AsF_6]·2XeF_2 as 2HOXeF·[H_3O][AsF_6] or [H_2OXeF]$_2$[F][AsF_6] were ruled out because of the absence of ^{18}O and D isotopic shifts for the 552 and 470 cm^{-1} bands in the experimental Raman spectra of [$H_3{}^{18}O$][AsF_6]·2XeF_2 and [D_3O][AsF_6]·2XeF_2. Furthermore, the lack of agreement between the observed and calculated harmonic frequencies for the H_2OXeF^+ cation and HOXeF eliminate these species as possible constituents of the solid. In addition, failure to observe the ^{18}O isotopic shifts, predicted computationally, also ruled out this species (see Computational Results).

Nuclear Magnetic Resonance Spectroscopy. Fluorine-19, ^{129}Xe, and ^{17}O NMR spectra were recorded unlocked (field drift <0.1 Hz h^{-1}) on a Bruker DRX-500 spectrometer equipped with an 11.744-T cryomagnet and a Bruker 10 mm broadband probe. The NMR probe was cooled using a nitrogen flow and variable-temperature controller (BV-T 3000). For NMR spectroscopic characterization, samples were loaded into 9-mm FEP tubes heat-fused to a ca. 5-cm length of 0.25-in. FEP, which in turn was connected to a Kel-F valve, subsequently heat-sealed under dynamic vacuum at −196 °C, and inserted into a thin wall precision glass 10-mm NMR tube (Wilmad). Fluorine-19 NMR spectra acquired while monitoring the reaction of XeF_2 with [H_3O][AsF_6] in BrF_5 solvent were recorded unlocked ((field drift <0.1 Hz h^{-1}) on a Bruker AC-300 spectrometer using a Bruker 5-mm ^{1}H/^{13}C/^{19}F/^{13}C QNP probe. Samples in 4-mm FEP tubes were heat sealed under dynamic vacuum at −196 °C and inserted into a thin wall precision glass 5-mm NMR tube (Wilmad).

The ^{19}F, ^{129}Xe, and ^{17}O NMR spectra of a sample of [XeF][AsF_6] and ^{17}O-enriched H_2O (HF solvent at −75 °C) were acquired at 470.477, 138.867, and 67.811 MHz in 64 K, 32 K, and 32 K memories with spectral settings of 150, 100, and 100 kHz, yielding acquisition times of 0.218, 0.164, and 0.164 s and data point resolutions of 2.29, 3.05, and 3.05 Hz/data point, respectively. The number of transients accumulated for the ^{19}F, ^{129}Xe, and ^{17}O NMR spectra was 721, 363, and 5253 using a pulse width of 2.5, 10, and 10 μs, respectively.

The reaction of [H_3O][AsF_6] and XeF_2 in BrF_5 solvent was monitored by ^{19}F NMR spectroscopy, with spectra acquired at 282.409 MHz (AC-300), followed by an acquisition at 470.477 (DRX-500) when the reaction was deemed to be complete (values in parentheses), in 32 (64) K memory with a spectral setting of 100 (100) kHz yielding an acquisition time of 0.164 (0.328) s and data point resolution of 6.104 (1.53) Hz/data point using a pulse width of 4.0 (2.5) μs. The number of transients accumulated was 4100 (1000).

The ^{17}O, ^{19}F, and ^{129}Xe NMR spectra were referenced externally at 30 °C to samples of neat H_2O, $CFCl_3$, and $XeOF_4$, respectively. The chemical shift convention used is that positive (negative) sign indicates a chemical shift to high (low) frequency of the reference compound.

Raman Spectroscopy. Raman spectra were obtained directly in the FEP reaction vessel using two different Raman spectrometers: (a) a Cary Model 83GT using the 488-nm line of a Lexel Model 95 Ar^+ laser and (b) a Bruker RFS 100/S FT Raman spectrometer using 1064-nm excitation as previously described.[48] As previously described, low-temperature spectra on the Cary and the Bruker spectrometers were recorded using a macrochamber[57] and a Bruker low-temperature accessory,[51] respectively.

Infrared Spectroscopy. Infrared spectra were recorded in the range 300−4000 cm^{-1} on a Midac Model M FTIR spectrometer. Spectra of solids were obtained by using dry powders pressed between AgCl windows in an Econo press (Barnes Engineering Co.). For the low-temperature spectra, the cold sample was placed between cold AgCl windows inside the drybox. The windows were mounted in a liquid-nitrogen-cooled copper block mated with an O-ring flange to an evacuable glass cell equipped with outer CsI windows.[58]

Computational Methods. Electronic structure calculations were carried out using DFT (SVWN, BP86, B3LYP, B3PW91, PBE1PBE and MPW1PW91) and ab initio (MP2 and CCSD(T)) methods using the program Gaussian 03 (version C.02). The aug-cc-pVDZ, and aug-cc-pVTZ[45] basis sets as implemented in the Gaussian program were utilized for all elements except Xe, for which the semirelativistic small core pseudopotential basis sets aug-cc-pVDZ-PP and aug-cc-pVTZ-PP were used. The combined use of aug-cc-pV*n*Z and aug-cc-pV*n*Z-PP basis sets is indicated as aug-cc-pV*n*Z(-PP). All DFT and MP2 calculations were performed at McMaster University, and the CCSD(T) calculations were performed at Edwards Air Force Base. The program GaussView was used to visualize the vibrational displacements that form the basis of the vibrational mode descriptions given in Tables 4, 5, S3, and S5−S8). Nuclear magnetic resonance shielding tensors were calculated by the GIAO-MBP2 method using CCSD(T)/aug-cc-pVDZ optimized geometries.

Acknowledgment. We thank the Natural Sciences and Engineering Research Council of Canada for support in the form of a Discovery Grant (G.J.S.) and for the award of postgraduate scholarships (M.G. and M.D.M.). Furthermore, we thank McMaster

---

(56) Farrugia, L. *J. Appl. Crystallogr.* **1999**, *32*, 837–838.

(57) Miller, F. A.; Harney, B. M. *Appl. Spectrosc.* **1970**, *24*, 291–292.

(58) Loos, K. R.; Campanile, V. R.; Goetschel, T. C. *Spectrochim. Acta, Part A* **1970**, *26A*, 365.

University for the award of James A. Morrison Memorial Scholarships and the Ontario Ministry of Education and Training for the award of Ontario Graduate Scholarships (M.G. and B.E.P.) and for the award of a Richard Fuller Memorial Scholarship (M.G.). The authors also thank David S. Brock for improving the synthesis and Raman spectrum of $[Xe_3OF_3][SbF_6]$. The quantum-chemical calculations carried out at McMaster were made possible by the facilities of the Shared Hierarchical Academic Research Computing Network (SHARCNET: www.sharcnet.ca). The work at USC was supported by the National Science Foundation under Grant Nos. CHE-9985833 and CHE-0456343, the Air Force Office of Scientific Research, and the Office of Naval Research. We also thank the Deutsche Forschungsgemeinschaft for a Stipend (B.H.), Dr. J. Sheehy, Edwards Air Force Base, for some of the quantum-chemical calculations, and Prof. George A. Olah for his steady support.

Supporting Information Available: Views of $[Xe_3OF_3][PnF_6]$ (Pn = As, Sb) (Figures S1 and S2); factor-group analyses for $[Xe_3OF_3][PnF_6]$ (Pn = As, Sb) (Tables S1 and S2); calculated vibrational frequencies and geometrical parameters for $Xe_3OF_3{}^+$ using the aug-cc-pVDZ(-PP) basis set (Tables S3 and S4); calculated vibrational frequencies for $[H_3O][AsF_6]\cdot nXeF_2$ (n = 1−4) (Table S5); calculated geometries, frequencies and infrared intensities for symmetric and asymmetric XeF_2 (Table S6); calculated vibrational frequencies and geometrical parameters for HOF (Table S7), H_2OF^+ (Table S8), and FXeOH and for H_2OXeF^+ (Table S9); benchmark computational studies for XeF_2 (Table S10); calculated XeF^+ affinities (Table S11); absolute energies for all computed species (Table S12); X-ray crystallographic files in CIF format for the structure determinations of $[Xe_3OF_3][PnF_6]$ (Pn = As, Sb) and $[H_3O][AsF_6]\cdot 2XeF_2$. This material is available free of charge via the Internet at http://pubs.acs.org.

JA905060V